J. Fluid Mech. (2014), *vol.* 746, *pp.* 405–436. © Cambridge University Press 2014
doi:10.1017/jfm.2014.119

Steady turbulent density currents on a slope in a rotating fluid

G. E. Manucharyan[1,†], W. Moon[1], F. Sévellec[1,2], A. J. Wells[1,3], J.-Q. Zhong[1,4] and J. S. Wettlaufer[1,3]

[1]Yale University, New Haven, CT 06520, USA

[2]University of Southampton, Southampton SO14 3ZH, UK

[3]University of Oxford, Oxford OX1 3PU, UK

[4]Tongji University, Shanghai 200092, PR China

(Received 27 June 2013; revised 14 February 2014; accepted 27 February 2014; first published online 2 April 2014)

We consider the dynamics of actively entraining turbulent density currents on a conical sloping surface in a rotating fluid. A theoretical plume model is developed to describe both axisymmetric flow and single-stream currents of finite angular extent. An analytical solution is derived for flow dominated by the initial buoyancy flux and with a constant entrainment ratio, which serves as an attractor for solutions with alternative initial conditions where the initial fluxes of mass and momentum are non-negligible. The solutions indicate that the downslope propagation of the current halts at a critical level where there is purely azimuthal flow, and the boundary layer approximation breaks down. Observations from a set of laboratory experiments are consistent with the dynamics predicted by the model, with the flow approaching a critical level. Interpretation in terms of the theory yields an entrainment coefficient $E \propto 1/\Omega$ where the rotation rate is Ω. We also derive a corresponding theory for density currents from a line source of buoyancy on a planar slope. Our theoretical models provide a framework for designing and interpreting laboratory studies of turbulent entrainment in rotating dense flows on slopes and understanding their implications in geophysical flows.

Key words: gravity currents, rotating flows, turbulent mixing

1. Introduction

Fluids with horizontal density differences in a gravitational field will propagate to release the stored potential energy of their initial configuration. Such flows, variously referred to as density, gravity or buoyancy currents, are ubiquitous in geophysical, astrophysical and engineering settings (e.g. Simpson 1997; Huppert 2006; McKee & Ostriker 2007; Monaghan 2007), and a principal goal in their study revolves around predicting their rate of propagation given the initial geometry and density difference. Mixing plays an important role in turbulent currents, with the flow dynamics strongly influenced by exchanges of mass and momentum with the ambient fluid. Such is the case in many turbulent atmospheric and oceanic flows, including dense overflows

† Email address for correspondence: georgy.manucharyan@yale.edu

https://doi.org/10.1017/jfm.2014.119 Published online by Cambridge University Press

in the ocean (e.g. Smith 1975; Price & Baringer 1994) and landfalling cold fronts in the atmosphere (e.g. Garratt, Howells & Kowalczyk 1989), but these share much of the same basic physical mechanisms at play during star formation and within turbulent accretion discs (e.g. Rieutord & Zahn 1995; Lignieres, Catala & Mangeney 1996; Youdin & Shu 2002). As a particular example, dense overflows in ocean basins represent important components of the circulation, but the relevant mixing processes occur on length scales that are unresolved in climate models (e.g. Price & Baringer 1994; Ivanov *et al.* 2004). Hence, dynamically informed parameterisations are required to characterise buoyancy-driven currents. For flow down a slope from a persistent source of buoyancy flux, the initial transient propagation of the head of the current is driven by downslope differences in hydrostatic pressure across the density front (e.g. Shapiro & Zatsepin 1997; Wobus *et al.* 2011), whilst the downslope component of the gravitational body force becomes more significant in the subsequent phase of quasi-steady propagation. It is the latter, steady phase of propagation that we shall focus on here.

When the length and time scales are appropriate, the problem is complicated by the presence of the Earth's rotation, which puts additional constraints on the dynamics of currents and on the efficiency of turbulent entrainment (Griffiths 1986). An important consequence of rotation is that large-scale density currents running down the continental shelves get deflected by the Coriolis forces and eventually tend to propagate along the isobaths (Griffiths 1986), which are contours of constant depth. The flow along an isobath is considered to be in geostrophic balance with the Coriolis force balancing the pressure gradient force. However, it has been argued that frictional forces associated with bottom Ekman layers play a key role in breaking geostrophic balance and allowing a component of the current to cascade downwards (see Shapiro & Hill 1997, for example). Wirth (2009) pointed out that such density currents consist of a main thick current (or vein) and a thin frictional layer below it. For flows with negligible inertia and no entrainment, Wirth (2009) showed that the dynamics of the vein is mainly geostrophic but is modified by the presence of an Ekman layer. The Ekman layer leads to drainage of fluid from the vein into the frictional layer where it falls downslope and eventually mixes with the surrounding water. As a result, the main current slowly drifts downslope and its trajectory can be used to estimate the frictional drag (Wirth 2011). In this study we focus on the dynamics of the vein and in particular on how mixing processes affect its trajectory before reaching any geostrophically balanced state.

Mixing of ambient fluid into a dense current is often characterised in terms of an entrainment ratio $E = w_e/U$, i.e. the ratio of a mean inflow w_e normal to the interface to the mean velocity of the current U, itself depending on the instantaneous density and hence mixing. This entrainment hypothesis, introduced in the modelling of turbulent plumes (Morton, Taylor & Turner 1956), underlies many models of turbulent buoyancy-driven currents (see Turner 1986 for a survey). Such mixing can play a critical role not only in the trajectory and dynamics of a particular dense current but also in the maintenance of stratification in the interior of an ocean basin via the 'filling box' mechanism of Baines & Turner (1969). For example, Hughes & Griffiths (2006) and Wåhlin & Cenedese (2006) suggested that weak yet persistent entrainment into dense overflows could play a leading-order role in controlling the structure of the thermocline in the ocean interior. In the Arctic, a halocline separates warm, deep waters from the colder, fresher surface ocean and provides a barrier to vertical heat transfer that could melt the overlying sea-ice cover (Carmack 2000; Timmermans *et al.* 2009). The analysis and laboratory experiments of Wells & Wettlaufer (2007)

https://doi.org/10.1017/jfm.2014.119 Published online by Cambridge University Press

suggested that mixing rates can control whether dense currents will penetrate the halocline and ventilate the deep ocean or intrude into the halocline and maintain the stratification via the 'filling box' mechanism. Hence, mixing in dense currents provides an important contribution to the evolution of ocean stratification and, via the potential for feedback on sea-ice melting, to the state of the climate system as a whole.

The entrainment ratio E has been parameterised on the basis of a range of laboratory data and field observations; see Turner (1986) and Wells, Cenedese & Caulfield (2010) for reviews. For currents of thickness h, reduced gravity g' and viscosity ν, flowing on a slope at angle α to the horizontal, the data show that entrainment increases with both the Reynolds number $Re = Uh/\nu$, which characterises the vigour of turbulence, and the Froude number $Fr = U/\sqrt{g'h\cos\alpha}$, which characterises the tendency for shear-driven mixing to overcome the stabilising effect of stratification. (Note that some studies use the Richardson number $Ri = Fr^{-2}$.) Here U represents the relevant velocity scale along the slope, and for flows in pure geostrophic balance it would correspond to the Nof velocity $U_{geo} \sim g' \tan\alpha/f$, where f is the Coriolis parameter (Nof 1983; Wells 2007). The dependence of E on Fr and Re across a compilation of both rotating and non-rotating experiments and field measurements has been characterised by the empirical parameterisation of Cenedese & Adduce (2010). Alternatively, Wells *et al.* (2010) constructed a theory using a flux coefficient, which measures the ratio of buoyancy flux to viscous dissipation. This results in a scaling $E = A(Re, \alpha)Fr^n$, where the prefactor $A(Re, \alpha)$ depends on the Reynolds number and the slope angle. The exponent n captures a variety of scalings, with $n \to 0$ for $Fr \gg 1$, $n \sim 2$ for $Fr \sim 1$ and $n \gg 1$ for $Fr \ll 1$, which is consistent with the trend in the observations. However, there is some scatter in the data about the mean trend, and in particular observations indicate a substantial increase in mixing for larger Reynolds numbers (Princevac, Fernando & Whiteman 2005; Cenedese & Adduce 2010; Wells *et al.* 2010). This scatter could be due to intrinsic dynamical variability of turbulent entrainment about a mean value, the technical challenges of measuring entrainment, or differences in entrainment depending on the dynamical source of turbulence.

The previously described measurements of the entrainment parameter E rely on a variety of methods. In the absence of rotation, measurements of full velocity profiles allow E to be determined directly from mass conservation both for the flow of dense salty water on a laboratory-scale slope (Ellison & Turner 1959) and in field observations of katabatic winds (Princevac *et al.* 2005). An alternative approach constrains theoretical predictions using readily measured experimental features, such as the evolution of the background stratification in a filling box (Wells & Wettlaufer 2005). This allows a value of E to be inferred that is dynamically consistent with theory, and accounts for downslope evolution of the flow without requiring detailed measurements of velocity profiles. Entrainment into dense rotating currents in the ocean has been estimated from changes in the mass flux between two or more points on the path of the current (see Cenedese & Adduce 2010 for a summary). Laboratory studies of rotating currents have estimated entrainment from the increase in volume of the current between the source and the base of the tank (Cenedese *et al.* 2004; Wells 2007; Cenedese & Adduce 2008). In order to determine a value for E, a characteristic velocity scale is identified and assumed constant along the length of the flow. For example, Wells (2007) identified a velocity scale from the initial mass flux, whilst Cenedese *et al.* (2004) and Cenedese & Adduce (2008) used the propagation speed of the initial unsteady density front that is driven by downslope variations of hydrostatic pressure and precedes the subsequent steady flow driven by the downslope

https://doi.org/10.1017/jfm.2014.119 Published online by Cambridge University Press

component of gravity. For these measurements in rotating systems, it is plausible that variations of the downslope velocity between measurement points may contribute to the scatter of the measured E values around the parameterisations of Cenedese & Adduce (2010) and Wells *et al.* (2010). Motivated by this background, we developed a theoretical model for steady flow of a turbulent rotating density current down a conical sloping surface. The approach accounts for downslope development of the flow and provides a framework for systematic studies of entrainment dynamics in well-characterised laboratory experiments.

In the next section we formulate the problem of a shelf-slope system in which a density current is delivered onto the surface of a cone, considering both axisymmetric flow and isolated currents of finite angular extent. The essence of the problem can be thought of as a steady rotating version of the model of Morton *et al.* (1956) but with bottom friction associated with the fact that our 'plume' is a current on a slope (Ellison & Turner 1959). In § 3 we determine numerical solutions for a representative laboratory set-up, as well as analytical solutions for a dense current from an initial buoyancy source where the initial fluxes of mass and momentum are small and dynamically negligible, along with a first-order asymptotic correction to account for the initial mass and momentum fluxes. The attractor solution qualitatively reproduces the asymptotic behaviour of the numerical solutions away from the source, and allows us to characterise the parametric dependence of the flow on entrainment. The linearised asymptotic correction is necessary to account for the initial conditions and provide a good quantitative approximation to the numerical solutions across the full length of the flow. A set of experiments is described in § 4, demonstrating how the theory captures the correct flow structure and allows us to estimate how the turbulent entrainment varies with rotation rate, which we explore in detail in § 5. The work is summarised in § 6, where we describe ongoing experimental research and implications for future studies.

2. Formulation of the model

The model considers fluid of density $\tilde{\rho}$ introduced onto the surface of a solid cone of slope angle α to the horizontal, immersed in a background fluid of uniform density ρ_0, as illustrated in figure 1. The system rotates with angular velocity Ω parallel to both gravity g and the vertical. With flow confined below the apex of the cone, we use an orthogonal coordinate system relative to the conical surface, with s representing the distance downslope parallel to the conical surface, η the distance normal to the cone and θ the azimuthal angle. The local velocity components in each direction are $\boldsymbol{u} = (u_s, u_\eta, u_\theta)$.

2.1. *Plume model for a density current on a cone*

The governing equations for the density current flow in a rotating reference frame are derived from first principles in appendix A. The approach follows that of Morton *et al.* (1956) and Ellison & Turner (1959) to derive plume equations for the downslope fluxes. This method of modelling uses depth-integrated budgets to describe the turbulent core of the current (described as the 'vein' by Wirth 2009) and does not explicitly resolve the viscous Ekman layers. The consistency of this assumption is discussed in § 6. Note that this modelling approach can incorporate frictional effects from the Ekman layer in a drag parameterisation for the basal shear stress, as discussed below. In contrast to earlier streamtube models (such as e.g. Smith 1975), we develop a theory specific to conical geometry that allows analytical progress to

https://doi.org/10.1017/jfm.2014.119 Published online by Cambridge University Press

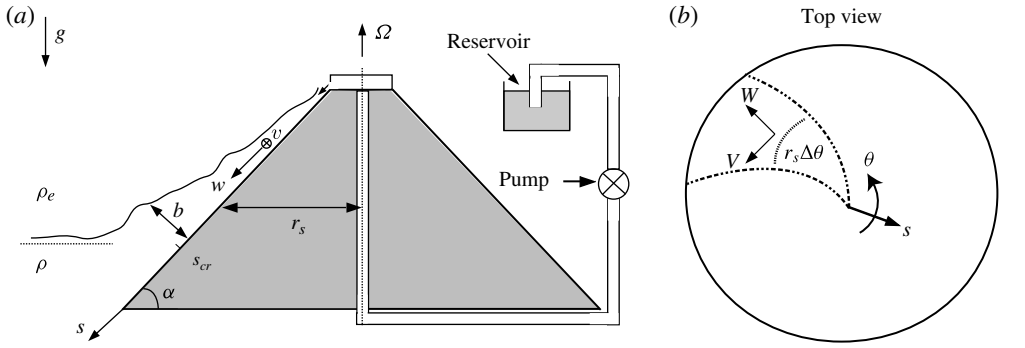


FIGURE 1. Schematic view of the density current on a cone in a rotating fluid, as described in the main text: (*a*) view from the side, indicating the system geometry, notation and experimental set-up; (*b*) view from above for a current with effective angular extent $\Delta\theta$.

be made with the goal of analysing turbulent mixing in experimental studies. For flow of angular extent $\Delta\theta$ over the surface of the cone as illustrated in figure 1(*b*), the conservation equations of mass, vertical momentum, azimuthal momentum and buoyancy are given by

$$\frac{\mathrm{d}}{\mathrm{d}s}\left(\Delta\theta r_s b w\right) = \Delta\theta r_s v_e, \tag{2.1}$$

$$\frac{\mathrm{d}}{\mathrm{d}s}\left(\Delta\theta r_s b w^2\right) = \Delta\theta r_s b g \sin\alpha \frac{\rho-\rho_0}{\rho_0} - \Delta\theta r_s b f v + \Delta\theta b v^2 \cos\alpha - \frac{\tau_s}{\rho_0}\Delta\theta r_s, \tag{2.2}$$

$$\frac{\mathrm{d}}{\mathrm{d}s}\left(\Delta\theta r_s b w v\right) = \Delta\theta r_s b f w - \Delta\theta b v w \cos\alpha - \frac{\tau_\theta}{\rho_0}\Delta\theta r_s \tag{2.3}$$

and

$$\frac{\mathrm{d}}{\mathrm{d}s}\left(\Delta\theta r_s b w \frac{\rho-\rho_0}{\rho_0}\right) = 0, \tag{2.4}$$

where the effective plume width b, mean plume velocity (w, v) and mean density ρ are defined in terms of the fluxes

$$\int_0^{2\pi}\int_0^{\infty} r u_s \,\mathrm{d}\eta\,\mathrm{d}\theta \equiv b r_s w \Delta\theta, \tag{2.5}$$

$$\int_0^{2\pi}\int_0^{\infty} r u_s^2 \,\mathrm{d}\eta\,\mathrm{d}\theta \equiv b r_s w^2 \Delta\theta, \tag{2.6}$$

$$\int_0^{2\pi}\int_0^{\infty} r u_\theta u_s \,\mathrm{d}\eta\,\mathrm{d}\theta \equiv b r_s v w \Delta\theta \tag{2.7}$$

and

$$\int_0^{2\pi}\int_0^{\infty} r u_s \frac{\tilde{\rho}-\rho_0}{\rho_0}\,\mathrm{d}\eta\,\mathrm{d}\theta \equiv b w r_s \frac{\rho-\rho_0}{\rho_0}\Delta\theta, \tag{2.8}$$

where $r_s = s\cos\alpha$ is the local radius of the cone, $f = 2\Omega\cos\alpha$ is the Coriolis parameter, $r = s\cos\alpha + \eta\sin\alpha$, and we have assumed self-similar profiles for u_s,

https://doi.org/10.1017/jfm.2014.119 Published online by Cambridge University Press

u_θ and $\tilde{\rho} - \rho_0$ when determining the buoyancy-force term and Coriolis-force term, as discussed in appendix A. For axisymmetric flow the angular extent is $\Delta\theta = 2\pi$, whilst for flows of finite angular extent $\Delta\theta$ must be specified separately, as discussed in § 2.2. To close the model, we must specify the entrainment velocity v_e and the shear stress at the base, $\boldsymbol{\tau} = (\tau_s, \tau_\theta)$. We extend the entrainment criterion of Morton *et al.* (1956) to account for two velocity components by assuming that the entrainment velocity is proportional to the mean speed of the current on the slope,

$$v_e = E\sqrt{v^2 + w^2}, \tag{2.9}$$

where E is the entrainment coefficient. For large-Reynolds-number flow, the turbulent drag is dominated by eddy momentum fluxes, with the eddy velocity determined from the mean flow speed. Hence we set

$$\frac{\boldsymbol{\tau}}{\rho_0} = K\sqrt{v^2 + w^2}\,(w, v), \tag{2.10}$$

where K is the friction coefficient (Taylor 1920). In § 6 we discuss the impact of an alternative drag parameterisation that approximates Ekman veering. Ekman layer dynamics may also lead to a leakage of fluid from the main core of the current, which can be described by an additional mass sink added to (2.5) following Wåhlin & Walin (2001). However, based on the analysis of Wåhlin & Walin (2001) for geostrophic flows, we expect this Ekman mass flux to be small whenever $\delta_{Ek} \ll b$ so that the Ekman-layer thickness is small compared to the depth of the current. In the subsequent analysis, we neglect this Ekman flux and revisit the assumption in § 6.

For axisymmetric flow with $\Delta\theta = 2\pi$, the resulting equations (2.1)–(2.10) yield a closed system of four ordinary differential equations, which are solved with initial conditions for prescribed values of b, w, v and ρ at a particular distance s_I close to the top of the cone. In addition to seeking analytical solutions, the system was integrated numerically using forward Euler time-stepping, with convergence confirmed as the discretisation step $\Delta s \to 0$.

2.2. *Density currents from isolated sources of confined angular extent*

The equations (2.1)–(2.10) are also a valid description of the flow of a single stream of fluid as illustrated in figure 1(*b*), once the angular extent $\Delta\theta$ has been specified. In appendix A we show that whenever the variation of the angular extent $\Delta\theta$ is sufficiently small (according to (A 19)), a single-stream flow can be described by a subsection of constant angle $\Delta\theta$ of the corresponding axisymmetric flow. Hence, when changes in $\Delta\theta$ are small, the trajectory of the centre-line of a single-stream flow is given by a path-line of the axisymmetric solution. Changes in $\Delta\theta$ can be driven either by the force resulting from lateral gradients in hydrostatic pressure at the edge of the current, or by the widening of the current via turbulent entrainment along the current sides. To estimate the influence of changing $\Delta\theta$ in the model, we computed an "indicator" $\mathrm{d}(\ln \Delta\theta)/\mathrm{d}(\ln s)$. This approximate indicator estimates the relative magnitude of terms neglected from the model that arise from changes in $\Delta\theta$, as compared to terms retained in the model that describe downslope variation of mass and momentum fluxes (see the discussion of criterion (A 19) in appendix A for a theoretical rationale for this indicator). We estimate that the neglected terms are likely to be insignificant whenever $\mathrm{d}(\ln \Delta\theta)/\mathrm{d}(\ln s) \ll 5/3$. For a sample experimental current path without rotation, the resulting change in $\Delta\theta$ has only a moderate effect

https://doi.org/10.1017/jfm.2014.119 Published online by Cambridge University Press

on the dynamics, with the average value $\overline{\mathrm{d}(\ln \Delta\theta)/\mathrm{d}(\ln s)} = 0.24$; so in the absence of any validated theoretical model for changes in $\Delta\theta$, we develop analytical solutions for constant $\Delta\theta$. Note that this approximation implicitly prevents rapid widening of the current in a hydraulic jump (Pratt, Riemenschneider & Helfrich 2007), and the assumption may need to be relaxed in alternative flow configurations.

An adaptation of the model to describe flow down a planar surface is described in appendix C. The solutions exhibit qualitatively similar dynamics to that of flow over an axisymmetric cone, which is discussed below.

3. Model solutions

The development of the axisymmetric flow described by (2.1)–(2.10) depends on the initial fluxes of mass, momentum and buoyancy, in addition to the entrainment parameter E and friction parameter K. Whilst the theory can describe a wide range of steady turbulent flows on conical slopes, ranging from pure momentum jets to buoyancy-driven wall plumes, in this paper we focus on initial conditions relevant to a buoyancy-driven overflow that is primarily controlled by the input buoyancy flux, with small initial fluxes of mass and momentum. We begin by illustrating the behaviour of a numerical solution of (2.1)–(2.10) in an example experimental setting, before deriving analytical solutions and a first-order asymptotic correction for a special case that reveals the essential features of the dynamics.

3.1. *General solution properties*

The thick black curves in figure 2 illustrate an example numerical solution of the plume model (2.1)–(2.10) that is representative of a laboratory setting, with initial fluxes of buoyancy, mass and momentum released some distance $s = s_I$ below the apex of the cone. The solution involves a critical point occurring at a particular depth $s = s_{cr}$. In the vicinity of this critical point, the downslope component of velocity approaches zero (see figure 2) as the flow approaches a state of purely azimuthal flow. In the framework of our steady-state axisymmetric plume model, there are no physical solutions beyond the critical point, and fluid is not allowed to penetrate below it. Hence the persistent flux of fluid results in a divergence of the modelled plume width. This leads to a breakdown of the boundary-layer approximation employed by the theory, which assumes that the current is thin compared to the along-slope extent, with additional physical processes becoming important in a small neighbourhood of the critical point. We thus expect that in laboratory experiments there will still be downslope leakage of dense fluid beyond the critical point. However, one should be able to observe an abrupt change in the behaviour of the flow as it approaches the critical level. At this juncture it is appropriate to note an analogy with critical levels for intrusion of plumes into stratified ambients (Morton *et al.* 1956). In the plume model of Morton *et al.* (1956), the flow is arrested at a critical point due to the stratification reducing the relative buoyancy force, with the inertia of the plume causing it to slightly overshoot the level of neutral buoyancy before the plume is decelerated. For rotating density currents the outward flow is arrested at a critical point by rotation, with the Coriolis forces counteracting the downslope buoyancy forces and stopping the downslope flow after the current overshoots a level where Coriolis and buoyancy forces are in geostrophic balance.

The path-line of a tracer particle released into the axisymmetric flow has no downslope component at the critical point s_{cr}. As illustrated by the thick black curves in figure 3(*a*), the trajectory $s = s(\theta)$ terminates at the critical point (where $w = 0$)

https://doi.org/10.1017/jfm.2014.119 Published online by Cambridge University Press

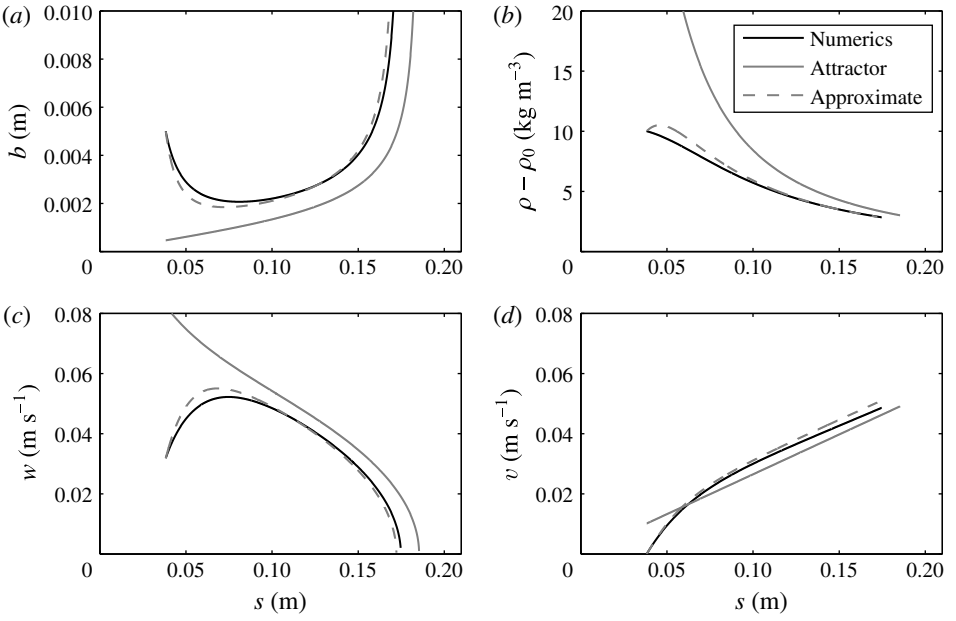


FIGURE 2. Flow development with distance s from the apex of the cone: (a) thickness; (b) density anomaly; (c) downslope velocity; (d) azimuthal velocity. The thick black solid curves represent the numerical solution of the full equation set (2.1)–(2.10), whilst thin grey curves show the asymptotic attractor solution (3.10)–(3.12) and dashed curves show the approximate solution including higher-order corrections (3.14) and (3.19)–(3.21). The downslope flow ceases at a critical point s_{cr} where $w \to 0$, $b \to \infty$ and the boundary layer approximation breaks down. The parameters used are representative of a laboratory experimental set-up, with $g = 9.8$ m s^{-2}, $\rho_o = 1000$ kg m^{-3}, $\Omega = 0.6$ rad s^{-1} and $\alpha = 36°$, and for illustration we set $E = 0.1 \sin\alpha$ (Wells & Wettlaufer 2005) and $K = 2 \times 10^{-3}$, consistent with the order of magnitude determined by Taylor (1920). The prescribed initial conditions at $s = 0.038$ m are $\rho = 1010$ kg m^{-3}, $b = 5 \times 10^{-3}$ m, $w = 3.2 \times 10^{-2}$ m s^{-1} and $v = 0$ m s^{-1}.

after traversing a finite angle around the cone, rather than $\theta(s) \to \infty$, because the azimuthal velocity v remains bounded on approach to the critical point. Note that this trajectory also corresponds to the centre-line of a single-stream flow of constant angular extent. Clearly, the trajectories depend on the entrainment ratio E, which we explore further in § 3.4.

3.2. *Attractor solution*

To shed light on the generality of the dynamics illustrated by the numerical solutions, we now derive an analytical solution to the full model (2.1)–(2.10) for initial conditions with a constant initial buoyancy flux and negligible initial fluxes of mass and momentum. We later demonstrate that this solution is an attractor for the flow dynamics with arbitrary initial fluxes. From (2.4) we immediately observe that the downslope buoyancy flux Q_B is conserved,

$$\Delta\theta r_s b w \frac{\rho - \rho_0}{\rho_0} g \sin\alpha = \Delta\theta \cos\alpha \, Q_B, \tag{3.1}$$

https://doi.org/10.1017/jfm.2014.119 Published online by Cambridge University Press

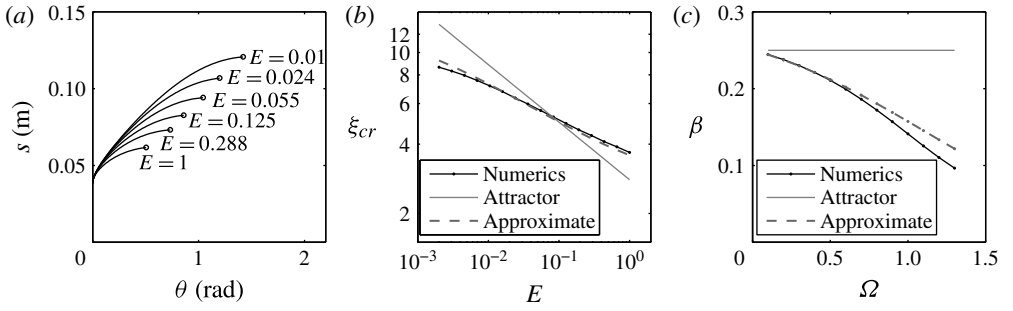


FIGURE 3. (*a*) Fluid parcel trajectories $s(\theta)$ from numerical solutions for a range of entrainment coefficients E, with $\Omega = 1$ rad s^{-1} and all remaining parameters as in figure 2; circles denote the critical points achieved at the end of the trajectories. (*b*) Sensitivity of the non-dimensional critical point $\xi_{cr} = s_{cr} f^{3/4} Q_B^{-1/4}$ to the entrainment coefficient E, plotted for $\Omega = 1$ rad s^{-1}; the numerical solution (thick black solid curve) is compared with the analytical scaling (3.22) for the attractor (thin grey curve) and the approximate solution (dashed curve) with higher-order corrections (3.14) and (3.19)–(3.21); note the logarithmic scales. (*c*) Approximate power-law exponent β plotted as a function of Ω (rad s^{-1}), where β is estimated from a power-law fit $\xi_{cr} = A E^{-\beta}$ to the curves in (*b*) and similar curves with different rotation rates, to approximate the sensitivity of the critical distance to entrainment; the numerical solution converges toward the attractor at small Ω.

with its value determined from the initial conditions. One could think of Q_B as the normalised integral mass flux of salt (or other density tracer) passing through a particular depth, which in the steady state has to be independent of depth to prevent accumulation of salt. It is natural to non-dimensionalise variables using Q_B and f, and so we introduce a dimensionless coordinate $\xi = s f^{3/4} Q_B^{-1/4}$ and define the new variables

$$P = \frac{sbwf^{5/4}}{Q_B^{3/4}}, \quad W = \frac{sbw^2 f}{Q_B}, \quad V = \frac{sbwvf}{Q_B}, \tag{3.2}$$

which represent dimensionless fluxes of mass, downslope momentum and azimuthal momentum, respectively, scaled by $\Delta\theta \cos\alpha$. Neglecting changes in $\Delta\theta$, the system (2.1)–(2.3) can be written as

$$\dot{P} = E\sqrt{W^2 + V^2}\,\frac{\xi}{P}, \tag{3.3}$$

$$\dot{W} = \frac{P}{W} - \frac{VP}{W} + \frac{V^2}{W\xi} - K\sqrt{W^2 + V^2}\,\frac{W\xi}{P^2} \tag{3.4}$$

and

$$\dot{V} = P - \frac{V}{\xi} - K\sqrt{W^2 + V^2}\,\frac{V\xi}{P^2}, \tag{3.5}$$

where a dot denotes $\mathrm{d}/\mathrm{d}\xi$. Note that the only remaining parameters in (3.3)–(3.5) are the entrainment coefficient E and the drag coefficient K.

https://doi.org/10.1017/jfm.2014.119 Published online by Cambridge University Press

It is useful to sum W times (3.4) and V times (3.5) and recast this system in terms of the variable $F = V^2 + W^2$:

$$\dot{P} = E\sqrt{F}\,\frac{\xi}{P}, \tag{3.6}$$

$$\dot{F} = 2P - 2K\frac{F^{3/2}\xi}{P^2} \tag{3.7}$$

and

$$\dot{V} = P - \frac{V}{\xi} - K\sqrt{F}\,\frac{V\xi}{P^2}. \tag{3.8}$$

For the special case of an initial point source of buoyancy at the apex of the cone, with no fluxes of mass or momentum, the initial conditions are

$$V = W = P = 0 \quad \text{at } \xi = 0, \tag{3.9}$$

so that $F(0) = 0$. Seeking power-law similarity solutions in ξ for P, F and V, we obtain

$$P = \frac{3}{2^{2/3}5^{2/3}}\frac{E^{2/3}}{\left(1+\frac{5}{4}\frac{K}{E}\right)^{1/3}}\xi^{5/3}, \tag{3.10}$$

$$F = \frac{9}{2^{8/3}5^{2/3}}\frac{E^{2/3}}{\left(1+\frac{5}{4}\frac{K}{E}\right)^{4/3}}\xi^{8/3} \tag{3.11}$$

and

$$V = \frac{9}{2^{2/3}5^{2/3}11}\frac{E^{2/3}}{\left(1+\frac{5}{4}\frac{K}{E}\right)^{1/3}\left(1+\frac{5}{11}\frac{K}{E}\right)}\xi^{8/3}, \tag{3.12}$$

which straightforwardly yield $b(s)$, $v(s)$, $w(s)$ and $\rho(s)$ upon algebraic manipulation. In appendix B we show that this solution is a unique attractor for the system of ordinary differential equations (3.6)–(3.8) with arbitrary initial conditions; that is, for sufficiently large s, the solutions (3.10)–(3.12) will approximate the leading-order asymptotic behaviour of any solution to (3.6)–(3.8). Note that we expect this attractor solution to provide a useful approximation when $s_I \ll s < s_{cr}$, which requires the critical level s_{cr} to be sufficiently far downstream of the initial level s_I.

In addition to the qualitative flow structure already discussed, two interesting features revealed by the leading-order attractor solution are the following. First, the resulting dimensional azimuthal velocity is $v \sim 3fs/(11 + 5K/E)$, which increases linearly with depth, has no explicit dependence on the buoyancy force and, for small friction coefficients, depends only weakly on the entrainment rate. Second, the downslope mass flux

$$\Delta\theta r_s bw \sim \Delta\theta\cos\alpha\,\frac{3}{2^{2/3}5^{2/3}}\frac{E^{2/3}}{\left(1+\frac{5}{4}\frac{K}{E}\right)^{1/3}}Q_B^{1/3}s^{5/3} \tag{3.13}$$

is independent of the rotation rate f (except via any implicit dependence of the entrainment parameter E on rotation).

https://doi.org/10.1017/jfm.2014.119 Published online by Cambridge University Press

Figure 2 compares the analytical attractor solution (thin grey curves) to the numerical solutions with small but non-zero initial fluxes of mass and momentum (thick black curves) relevant to an example experimental configuration. The attractor solution captures the qualitative behaviour of the numerical solutions, after an initial transient due to the experimental initial conditions not lying on the attractor. However, to achieve an improved quantitative comparison for initial conditions relevant to our experiments, it is useful to consider the next-order corrections to the asymptotic attractor solution (3.10)–(3.12) in order to account for the non-zero initial fluxes of mass and momentum in experimental settings.

3.3. *Linearised correction to the attractor solution*

Inspection of numerical solutions, such as those in figure 2, shows that for large rotation rates Ω the disagreement between the attractor solution and the numerical solution is large because the critical point $s = s_{cr}$ is reached before the solution has adjusted to the attractor. However, for $\Omega \to 0$ or $Q_B \to \infty$, (3.2) shows that the initial conditions P_0, V_0 and F_0 approach zero at $\xi = \xi_I \to 0$, thus recovering the initial conditions for the attractor solution. Hence, the attractor also acts as an asymptotic solution for small rotation rates or large buoyancy fluxes. We make use of this fact and calculate an approximate solution in the whole range of ξ using a generalised asymptotic expansion of the true solution around the attractor:

$$P = P_a + \hat{P}, \quad F = F_a + \hat{F}, \quad V = V_a + \hat{V}. \tag{3.14}$$

Taking $\hat{P} \ll P_a$, $\hat{F} \ll F_a$ and $\hat{V} \ll V_a$ and linearising (3.6)–(3.8) around the attractor solution, we find that

$$\frac{\mathrm{d}\hat{P}}{\mathrm{d}\xi} = \frac{10}{9\xi^2}\hat{F} - \frac{5}{3\xi}\hat{P}, \tag{3.15}$$

$$\frac{\mathrm{d}\hat{F}}{\mathrm{d}\xi} = 2\hat{P} \tag{3.16}$$

and

$$\frac{\mathrm{d}(\xi\hat{V})}{\mathrm{d}\xi} = \xi\hat{P}, \tag{3.17}$$

where we have set $K = 0$ for mathematical simplicity, which corresponds to neglecting bottom drag. For a typical value of $K = 10^{-3}$, this approximation results in only small quantitative differences from the full numerical solution, as illustrated in figure 2. Eliminating $\hat{P}$ from (3.15)–(3.16) leads to an Euler equation for $\hat{F}$,

$$\xi^2\frac{\mathrm{d}^2\hat{F}}{\mathrm{d}\xi^2} + \frac{5}{3}\xi\frac{\mathrm{d}\hat{F}}{\mathrm{d}\xi} - \frac{20}{9}\hat{F} = 0, \tag{3.18}$$

with solution

$$\hat{F} = A_1\xi^{\alpha_1} + A_2\xi^{\alpha_2}, \tag{3.19}$$

$$\hat{P} = \frac{A_1\alpha_1}{2}\xi^{\alpha_1} + \frac{A_2\alpha_2}{2}\xi^{\alpha_2} \tag{3.20}$$

https://doi.org/10.1017/jfm.2014.119 Published online by Cambridge University Press

and

$$\hat{V} = \frac{1}{2}\frac{A_1\alpha_1}{\alpha_1+1}\xi^{\alpha_1} + \frac{1}{2}\frac{A_2\alpha_2}{\alpha_2+1}\xi^{\alpha_2} + A_3\xi^{-1}, \tag{3.21}$$

where $\alpha_{1,2} = -1/3 \pm \sqrt{7/3}$ and the coefficients $A_{1,2,3}$ are determined from the initial conditions. We note here that if the initial conditions are far from the attractor, the constants $A_{1,2,3}$ would be $O(1)$ and thus the linearisation of the solution around the attractor would no longer be formally justified. Nonetheless, this method allows us to construct a solution that satisfies the initial conditions exactly and still preserves the asymptotic behaviour of the attractor solution as $\xi \to \infty$, since the perturbations grow more slowly than the attractor ($\alpha_{1,2} < 5/3$). Whilst a further correction could be made or the impact of small but non-zero K could be considered, this first-order correction provides sufficient accuracy over the experimentally motivated range of parameters that we consider in this paper. This is illustrated in figure 2 by the good agreement between this approximate solution (dashed curves) and the full numerical solution (thick black curves); see also figure 3.

3.4. *Sensitivity to entrainment*

Figure 3(*b*) illustrates the dependence of the non-dimensional value of the critical point $\xi_{cr} = s_{cr} f^{3/4} Q_B^{-1/4}$ on the entrainment rate E. It is clear that as turbulent entrainment increases, the distance to the critical point $s = s_{cr}$ decreases, which can be understood as a result of two effects. Increased entrainment of ambient fluid via turbulent mixing results in a decreased mean density of the mixture and hence a weakened buoyancy force. Furthermore, the ambient fluid has no momentum, and so increased entrainment dilutes the downslope momentum of the mixture. These effects combine to reduce the distance flowed downslope.

For cases where $s_{cr} \gg s_I$, we can estimate s_{cr} from the asymptotic solution (3.10)–(3.12). The critical depth s_{cr} is obtained when $W = 0$, which corresponds to $V^2 = F$ and yields

$$s_{cr} = \left(\frac{6655}{108}\right)^{1/4} \frac{\left(1 + \dfrac{5}{11}\dfrac{K}{E}\right)^{3/4}}{\left(1 + \dfrac{5}{4}\dfrac{K}{E}\right)^{1/4}} \left(\frac{Q_B}{Ef^3}\right)^{1/4}. \tag{3.22}$$

The friction parameter is typically small, with K of order 10^{-3} (Taylor 1920); and for $K/E \ll 1$, (3.22) yields the leading-order scaling $s_{cr} \propto E^{-1/4}$. Note that the dependence on the buoyancy flux Q_B and entrainment rate E is rather weak, but there is a stronger dependence on the Coriolis parameter f. For comparison, we note that the flow down a planar surface described in appendix C results in a scaling $s_{cr} \propto E^{-1/3}$.

As illustrated by the thin grey curve in figure 3(*b*), the scaling (3.22) from the asymptotic solution captures the leading-order magnitude of the numerical solution (thick black curve) for moderate values of E, of order 0.1, but does not capture the scaling behaviour with E. This disagreement arises because the numerical solutions are still influenced by the values of the initial condition and have not yet closely approached the attractor before s_{cr} is reached. After accounting for non-zero initial fluxes of mass and momentum using the first-order asymptotic correction, the approximate solution (dashed curve) produces much closer agreement with the

https://doi.org/10.1017/jfm.2014.119 Published online by Cambridge University Press

numerical solution, as seen in figures 2 and 3. Figure 3(*c*) illustrates the sensitivity of ξ_{cr} to entrainment for different rotation rates, by plotting the exponent β of a power-law fit $\xi_{cr} = AE^{-\beta}$ to data for different rotation rates Ω. For large Ω, the numerical solution (thick black curve) produces a power-law exponent β which differs markedly from the value $\beta = 0.25$ for the attractor solution (thin grey curve) expected from (3.22). The agreement improves markedly and the numerical scaling exponent approaches the attractor exponent as $\Omega \to 0$, consistent with the rationale described in § 3.3. The approximate solution (dashed curve), upon accounting for the full initial conditions via a linearised correction, produces much better agreement with the scaling exponent β observed in the numerical solutions. Hence, whilst the full solution of (2.1)–(2.10) approaches the asymptotic attractor solution (3.10)–(3.12) for large s, we conclude that the approximate linearised correction (3.14) and (3.19)–(3.21) may be required in experimental settings with large rotation rates where the initial fluxes of mass and momentum play a non-trivial role.

We have demonstrated that the modelled flow dynamics is sensitive to the entrainment parameter E, suggesting that an indirect measure of entrainment can be achieved in suitable experiments by observing flow quantities such as s_{cr}. This motivates a series of laboratory experiments to examine the theory discussed in this section and to investigate the effects of rotation on the effective entrainment rate.

4. Experimental comparison

4.1. *Experimental arrangement*

A set of laboratory experiments was conducted to investigate the dynamics of a single-stream turbulent flow of small angular extent. Consistent with the situation shown in figure 1, we consider flow on a truncated cone with slope angle $\alpha = 36°$ to the horizontal, maximum radius 18.4 cm and minimum radius $r_I = 3.1$ cm, so that $s_I = r_I/\cos\alpha = 3.8$ cm.

The cone was mounted at the centre and 4 cm above the base of a large tank of 100 cm × 100 cm square cross-section, allowing a large overflow region to minimise the influence of any 'filling box' effects in the far-field fluid over the course of an experiment. The tank was filled to a depth of 8 cm above the top of the truncated cone, to minimise the influence of an effective two-layer geostrophic flow induced by the input of dense fluid. Lane-Serff & Baines (1998) and Sutherland *et al.* (2004) showed that this effect is significant when the lower dense layer occupies an appreciable fraction of the total depth, and this contributes to the formation of large eddies.

The tank was spun up into an approximate state of solid-body rotation with angular velocity 0.4 rad $s^{-1} \leqslant \Omega \leqslant 1.3$ rad s^{-1} which was varied between experiments. This range of angular velocities was chosen for practical reasons. The lower limit prevents the lower edge of the current from approaching the edge of the cone as the current reaches the critical level s_{cr}, and also avoids difficulties in image processing due to a reduced signal-to-noise ratio as the current becomes more diluted. As the rotation rate was increased beyond 1.3 rad s^{-1}, we observed the onset of large-scale baroclinic instabilities which introduced large variance into the current trajectory, with safety considerations precluding further increases in rotation rate.

A dense NaCl–H_2O solution was dyed with potassium permanganate, with total density excess $\Delta\rho = \rho_i - \rho_e$ measured using an oscillating-type densitometer (Anton Paar DMA 3.5N). The dense fluid was introduced at the top of the cone via the following flow-injection mechanism. A pump supplied dense water at flow rates

https://doi.org/10.1017/jfm.2014.119 Published online by Cambridge University Press

Exp no.	Ω (rad s^{-1})	$\Delta\rho/\rho_e$	$Q_B(\times 10^{-7}$ m^{4}s$^{-3})$	$s_{cr}(\times 10^{-2}$ m)	E
1	0.40	0.0155	2.98	14.20	0.123
2	0.50	0.0154	1.99	11.55	0.111
3	0.50	0.0124	1.55	10.99	0.099
4	0.57	0.0129	1.62	11.91	0.043
5	0.57	0.0129	2.53	11.25	0.092
6	0.59	0.0124	1.55	11.05	0.049
7	0.63	0.0124	1.48	9.32	0.099
8	0.64	0.0124	1.58	9.73	0.074
9	0.66	0.0124	1.51	9.69	0.069
10	0.70	0.0154	2.15	9.81	0.083
11	0.74	0.0124	1.47	9.58	0.046
12	0.79	0.0154	2.00	9.19	0.073
13	0.84	0.0137	1.67	8.67	0.055
14	0.90	0.0124	1.48	8.85	0.033
15	1.00	0.0124	1.44	7.84	0.047
16	1.06	0.0124	1.55	7.47	0.057
17	1.15	0.0124	1.50	8.19	0.018
18	1.29	0.0124	1.51	7.77	0.016

TABLE 1. List of experimental conditions and derived quantities. The rotation rate Ω, initial normalised density difference $\Delta\rho/\rho_e$ and initial dimensional buoyancy flux $Q_B\Delta\theta$ supplied by the pump are imposed for each experiment, and the initial angular extent $\Delta\theta = 0.5$ rad is diagnosed from the data as described in the main text. The final two columns show the estimated critical distance s_{cr}, at which the downslope propagation of the core of the current stops, and the corresponding entrainment coefficient E inferred as a value that produces best agreement between the observed s_{cr} and a numerical solution, described further in the main text.

0.0185 cm^3 s^{-1} $< Q <$ 0.0305 cm^3 s^{-1} to an enclosed cylindrical 'pill box'-shaped reservoir of 3.1 cm radius and 1 cm depth. The pill-box reservoir was filled with glass beads and the piping was filled with sponge material so that flow through it acted to suppress small flow oscillations introduced by the pump. Dense fluid exited the pill-box reservoir via a cylindrical hole drilled adjacent and parallel to the cone surface. The small hole diameter $d = 0.5$ cm produces a sufficient initial velocity for the dense current to be initiated in a turbulent state with visible eddying motion. Earlier attempts with an axisymmetric flow release resulted in only unsteady laminar flow without significant eddy-driven mixing, because the flow rates of the available pump could not achieve a sufficiently high Reynolds number when spread over an axisymmetric source. Table 1 summarises the experimental parameters. Note that in determining the buoyancy flux Q_B given by (3.1) and appropriate to the theory, we estimate the angular extent $\Delta\theta$ of the current as described below.

4.2. *Structure of the current*

Plan-view images were recorded at a frame rate of 24 Hz for the approximate 500 s duration of an experiment using a digital camera mounted above the tank in the rotating frame and DigiFlow software (Dalziel Research Partners, Cambridge). Distribution of the greyscale intensity in the plan-view images also provides information concerning the density distribution in the current. The greyscale intensity increases with increased concentration of dye and fluid density. After a 45 s transient

https://doi.org/10.1017/jfm.2014.119 Published online by Cambridge University Press

period during which the flow develops, the subsequent 11 000 images were analysed using a custom-written MATLAB code. For further analysis the images were time-averaged over 10 inertial periods, where the inertial period is $1/(2\Omega)$, to smooth out the effects of small-scale eddies and to avoid shadow effects from the background lighting, thus obtaining time series of the large-scale variability of the density current. The initial angular extent of the current was estimated from the time-averaged greyscale colour intensity, by fitting a Gaussian profile $A\exp[-(\theta-\theta_0)^2/\sigma_\theta^2]$ to the data averaged over 3.6 cm $< r <$ 4.1 cm, a short distance beyond the initial contact of the current with the cone. We estimate the angular extent using $\Delta\theta = M\sigma_\theta$, with $M = 4$ chosen corresponding to the central 95 % of a Gaussian distribution. There is some arbitrariness in the choice of $\Delta\theta$, but we note that different values of M simply result in a uniform linear rescaling of all values of Q_B. Hence, whilst this rescaling may uniformly affect the absolute values of the entrainment parameter E inferred below, it does not influence the relative changes of E with Ω. We expect non-negligible errors associated with the nonlinearity of the mapping function between the pixel intensity and the density and thickness of the current as well as due to refraction effects. Thus, rather than estimating a value of $\Delta\theta$ for each experiment individually subject to large statistical fluctuations, we choose to use a constant value of $\Delta\theta = 0.50$ rad, which is an ensemble mean value over all the experiments (with ensemble standard deviation $\sigma(\Delta\theta) = 0.13$ rad).

Figure 4 shows an example of both the instantaneous and the time-averaged structure of the current, with the scale indicating changes in dye colour intensity extracted from the black-and-white images. For the rotation rates reported here, the dense current propagates both down the cone surface and azimuthally until a state of azimuthal flow is approached at $s = s_{cr}$. The core of the current approaches the critical level $s = s_{cr}$ (where the theory breaks down) after traversing an angle of order $\theta \sim 60°$, and there is strong downslope leakage in a thin unsteady laminar layer featuring roll waves but lacking any notable entraining eddy structures. This leakage leads to the current dispersing over the lower section of the cone surface. There is also weak downslope leakage in an Ekman layer along the length of the current, but image analysis allows us to extract the maximum dye colour intensity to track the turbulent entraining core of the current. We note here that the time-averaged current cannot transport buoyancy downslope across the critical level (because $w = 0$ there). The entire buoyancy flux supplied by the source is transported across the critical level by the subsequent transient leakage.

4.3. *Effective trajectories and critical depth*

In order to quantitatively analyse the flow, the following automated image processing algorithm was used to extract the path of the current and its temporal variability. Since the theoretical model describes the trajectory of a Reynolds-averaged flow, we split the original data into a sequence of images that are time-averaged over 10 inertial periods. For each time-averaged image (numbered with $j = 1, \ldots, J$), we estimate a flow centre-line path $R_j(\theta)$ by finding the maximum greyscale colour intensity on each $\theta =$ constant ray with 1° increments, using polar coordinates centred at the tip of the cone. A nine-point 'lowess' smoothing filter (Cleveland 1981) is then applied along the θ dimension to remove outliers from each of the trajectories $R_j(\theta)$. An example time-averaged trajectory $R(\theta) = \left[\sum_j R_j(\theta)\right]/J$ is shown as the white solid curve in figure 4(*b*), whilst figure 5 illustrates the variability of all individual subsample trajectories (thin grey curves) compared to the time-averaged trajectory (thick black curve). In figure 5, the standard deviation increases significantly on

https://doi.org/10.1017/jfm.2014.119 Published online by Cambridge University Press

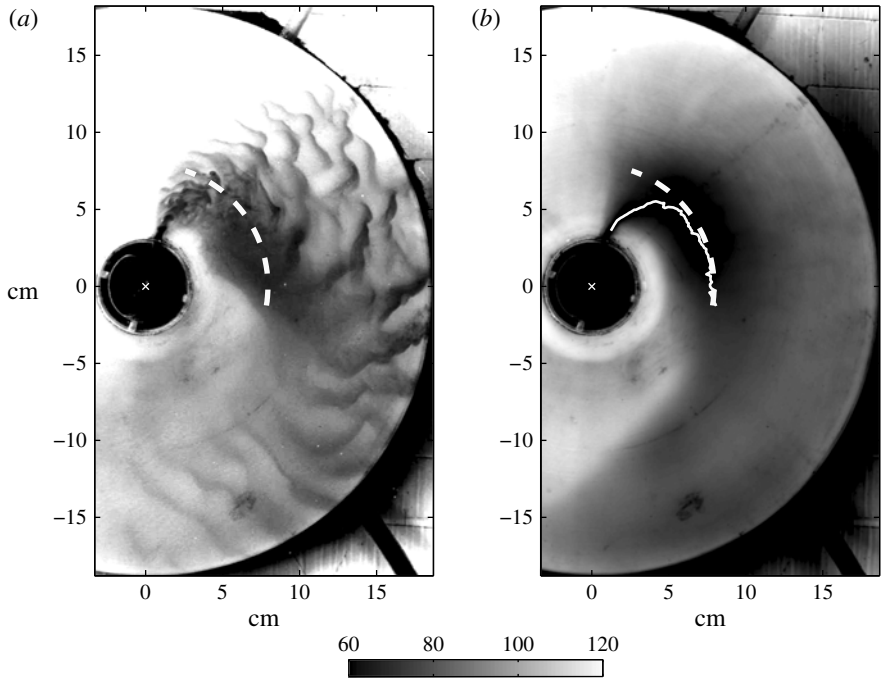


FIGURE 4. (*a*) A top-view snapshot of the single-stream density current for experiment no. 10 listed in table 1. (*b*) A corresponding image temporally averaged over 10 inertial periods. The scale shows the greyscale pixel intensity in the digital images, with regions of higher concentration of the dyed fluid in the descending dense current having darker intensity. Overlaid are the centre-line trajectory (white solid curve) and a critical level indicated by a white dashed circular arc with radius R_{cr}; the white cross in each panel denotes the axis of rotation.

approaching the region of smallest $\mathrm{d}R/\mathrm{d}\theta$ for $60° \lesssim \theta \lesssim 90°$, consistent with the breakdown of the theoretical model and leakage from the core of the current as the critical level is approached. As an objective and reproducible estimate of the distance at which the breakdown occurs, we first define an index $I_W(\theta) = (\mathrm{d}R/\mathrm{d}\theta)[Std(R)]^{-1}$, which is the slope of the trajectory normalised by the standard deviation $Std(R)$ due to temporal variability at each value of θ. The index has large values at the beginning of a trajectory and attains its first local minimum when the slope starts to diminish significantly and the variability of the current increases. We thus define the critical radius R_{cr} (and hence the critical downslope distance $s_{cr} = R_{cr}/\cos\alpha$) by fitting a horizontal line between the point of the first minimum in I_W and the remaining path up to an angle θ_{end}, after which the current is significantly diluted and the path-detection algorithm fails. The low-frequency temporal variability of the trajectories leads to uncertainties in determining s_{cr}, which we estimate using the standard deviation based on the difference between the mean path and the approximated horizontal line (figure 5).

4.4. *Critical point and entrainment estimates*

Figure 6(*a*) plots the dimensionless critical point $\xi_{cr} = s_{cr} f^{3/4} Q_B^{-1/4}$ for each experiment as a function of the rescaled dimensionless rotation rate $\hat{\Omega} = f s_I^{4/3} Q_B^{-1/3}$. Despite the

https://doi.org/10.1017/jfm.2014.119 Published online by Cambridge University Press

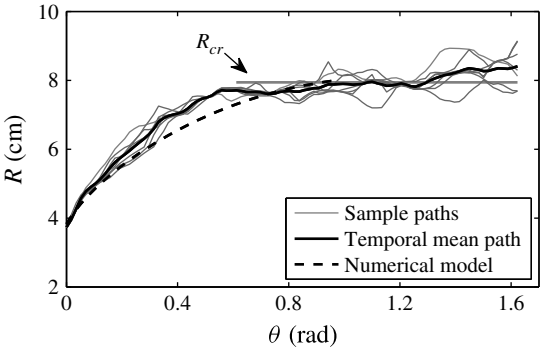


FIGURE 5. Reconstructed time-averaged trajectory given in polar form $R(\theta)$ (solid black curve) for experiment no. 10 listed in table 1, along with sample trajectories indicating time variability (grey curves). The level of R_{cr} is plotted starting from the value of θ at which the index I_W takes its first minimum (horizontal grey line). A numerical solution (dashed black curve) is obtained using the experimental initial conditions and the best-fit entrainment coefficient corresponding to the observed R_{cr}.

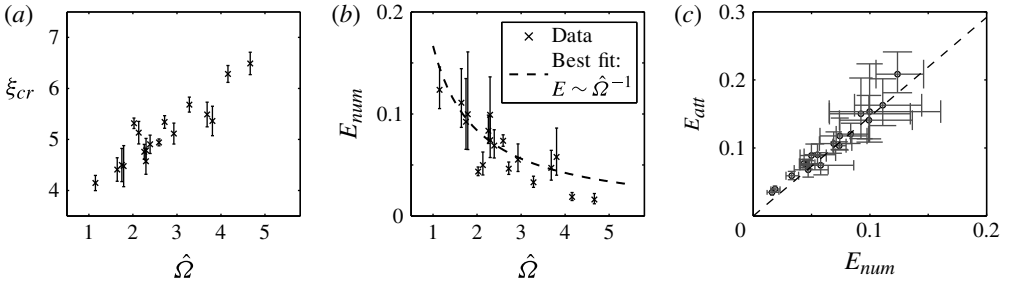


FIGURE 6. (*a*) Variation with the dimensionless rotation rate $\hat{\Omega} = fs_I^{4/3}Q_B^{-1/3}$ of the non-dimensional critical distance ξ_{cr}. (*b*) Variation with $\hat{\Omega}$ of the entrainment parameter E_{num} estimated so that a numerical integration of the full plume equations matches the observed value of ξ_{cr}; the best-fit scaling law $E \propto \hat{\Omega}^{-1.0}$ is plotted as a dashed curve. Error bars for ξ_{cr} in (*a*) are estimated from one standard deviation of the observed variability of ξ_{cr} over time, and these are used to estimate error bars for E in (*b*). (*c*) Comparison of E_{att} estimated from (3.22) with E_{num}, where the dashed line shows a linear fit $E_{att} = 1.46E_{num}$.

initial buoyancy flux varying between different experiments, as listed in table 1, the general trend clearly shows that ξ_{cr} increases as the rotation rate increases. We attribute this increase to the dependence of the entrainment coefficient on the rotation rate. As an attempt to quantify this, we investigate the consequences of assuming that the entrainment coefficient E is independent of s, so that a single value of E applies to each experiment. We firstly calculate an entrainment coefficient consistent with a numerical solution of the plume equations, using an optimisation routine that adjusts E to minimise the difference between the numerically obtained s_{cr} and the value based on experiments. The initial conditions for the numerical solutions are derived using the measured values described in table 1, combined with an estimated initial velocity scale $w_0 \approx Q_m/\pi d^2$ where Q_m is the measured initial mass flux and $d = 0.5$ cm is the diameter of the source nozzle. The velocity scale w_0 only factors into the estimate of the small initial momentum flux. In figure 6(*b*) we plot the value

https://doi.org/10.1017/jfm.2014.119 Published online by Cambridge University Press

of E so determined as a function of the dimensionless rotation rate $\hat{\Omega} = fs_I^{4/3}Q_B^{-1/3}$. Whilst the data show inherent scatter, they are consistent with the trend $E \propto 1/f$ indicated by the dashed curve. A power-law fit yields 95 % confidence bounds for the scaling exponent as $E \propto \hat{\Omega}^{-0.99\pm0.35}$ with an R-squared value of 0.69. This scaling has been determined empirically over the investigated range $0.65\ \mathrm{s}^{-1} \leqslant f \leqslant 2.1\ \mathrm{s}^{-1}$, with the experimental constraints preventing us from delimiting definitive upper and lower limits over which this scaling can be further extended. The entrainment values for experiments with low rotation rates are less well constrained due to large temporal variability of the currents. We indicate this variability with error bars calculated using the standard deviation of the spread in s_{cr} from the individual trajectories $R_j(\theta)$. Note that the attractor scaling (3.22) gives $E \propto s_{cr}^{-4}$, so we heuristically expect that the spread in E will be much larger than the spread in s_{cr}.

5. The dependence of entrainment on dimensionless groups

To investigate the robustness of the above result, we also considered an alternative estimate of entrainment, by inverting the attractor scaling (3.22) and using the observed s_{cr} to determine a value $E = E_{att}$. Figure 6(*c*) compares E_{att} to the estimate E_{num} based on a full numerical integration. The data can be approximated by a linear relationship $E_{att} = 1.46E_{num}$, showing that the attractor solution captures the trend of the variation of E between experiments but tends to overestimate its value relative to the full numerical solution. A power-law fit to this second estimate yields $E_{att} \propto \hat{\Omega}^{-1.05\pm0.24}$, which is also consistent with the trend $E \propto 1/f$ identified above. This suggests that the variation of E with f appears to be robust and independent of the choice of $M = 4$ in the estimate $\Delta\theta = M\sigma_\theta$: a different choice of M results in a uniform rescaling of Q_B in (3.22) and hence only modifies the proportionality constant in the trend $E_{att} \propto \hat{\Omega}^{-1.05\pm0.24}$ without changing the exponent.

The scaling dependence on the Coriolis parameter f and choice of dimensionless rotation rate is explored in further detail in figure 7. The Buckingham pi theorem requires that the entrainment parameter E depend only on non-dimensional quantities. The physical quantities characterising the attractor state are f, Q_B and the downslope coordinate s. Although in principle E could depend on the non-dimensional coordinate ξ, one cannot construct a constant non-dimensional group to characterise the significance of rotation for each experiment without invoking the initial conditions. The experimental initial conditions introduce the initial length scale s_I, along with additional fluxes of mass and downslope momentum, with the initial flux of azimuthal momentum being negligible. This leads to three independent dimensionless groups that depend on f, which can be characterised by (*a*) $\hat{\Omega} = \xi_I^{4/3} = fs_I^{4/3}Q_B^{-1/3}$, (*b*) P_0 defined using (3.2), and (*c*) W_0 defined using (3.2) (note that $V_0 \equiv 0$ is redundant). Figure 7(*a*) shows that the variation of E_{num} with $1/\hat{\Omega}$ is consistent with a linear trend, in support of the scaling $E \propto 1/f$. To investigate whether this trend captures the dominant variation with f, the renormalised quantity $E\hat{\Omega}$ is plotted versus $P_0^{-4/5}$ in figure 7(*b*) and versus W_0^{-1} in figure 7(*c*), where $P_0^{-4/5} \propto 1/f$ and $W_0^{-1} \propto 1/f$. The reduced quantity $E\hat{\Omega}$ shows no clear systematic dependence on $P_0^{-4/5}$ or W_0^{-1}, indicating that the scaling $E \propto 1/\hat{\Omega}$ captures the dominant variation with rotation rate. The results behave similarly for E_{att} (not shown), consistent with the broadly linear trend of $E_{att} \propto E_{num}$.

A scaling $E \propto 1/f$ was also observed in the experiments of Wells (2007) for axisymmetric flow on a rotating cone, which the author interpreted in terms of a

https://doi.org/10.1017/jfm.2014.119 Published online by Cambridge University Press

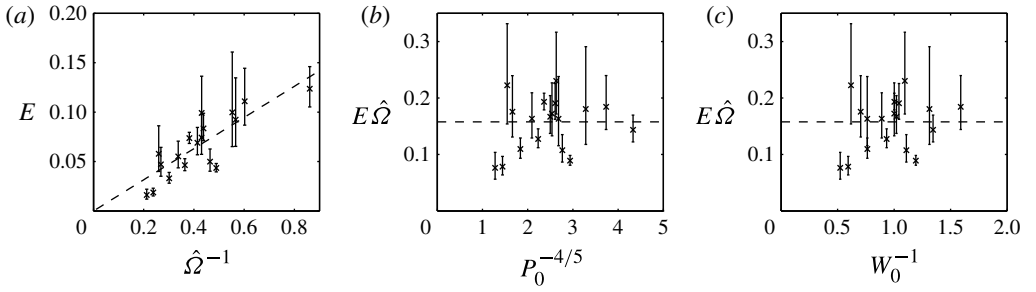


FIGURE 7. Investigation of the scaling of the entrainment rate E with the dimensionless groups $\hat{\Omega} = fs_I^{4/3}Q_B^{-1/3}$, P_0 and W_0 defined by (3.2), which depend on the rotation rate f: (*a*) variation of the scaled entrainment rate E with $\hat{\Omega}^{-1}$ (crosses with error bars, as in figure 6), which is consistent with a fitted linear trend $E = 0.16\,\hat{\Omega}^{-1}$, shown by the dashed line; (*b*) variation of the renormalised quantity $E\hat{\Omega}$ with $P_0^{-4/5} \propto 1/f$ (crosses with error bars); (*c*) variation of $E\hat{\Omega}$ with $W_0^{-1} \propto 1/f$ (crosses with error bars). Panels (*b*) and (*c*) indicate that the $E = 0.21\,\hat{\Omega}^{-1}$ trend (dashed line) captures the leading scaling with f, and there is no further systematic variation with the initial conditions P_0 or W_0.

scaling $E \propto Fr_{geo}$ where $Fr_{geo} = \sqrt{g'/h}\tan\alpha/f$ was calculated using the geostrophic Nof velocity $U_{geo} = g'\tan\alpha/f$ and the initial thickness h of the current. However, our theoretical model reveals the challenges associated with identifying a relevant Froude number for the entire trajectory of the flow, which evolves away from a state characterised by the initial thickness towards an attractor state that depends only on Q_B, f, α and s. There is no azimuthal velocity at the source, and hence the initial local Froude number $Fr_i = w_0/\sqrt{b_0 g_0' \cos\alpha}$ is characterised by the initial velocity w_0, current thickness b_0 and reduced gravity g_0', which are all independent of f. If the entrainment ratio E is constant, the flow then evolves towards the local Froude number in the attractor state,

$$Fr_{att} \equiv \frac{\sqrt{v^2+w^2}}{\sqrt{bg'\cos\alpha}} = \sqrt{\frac{5\tan\alpha}{4E+5K}}\left[1-\left(\frac{s}{s_{cr}}\right)^{8/3}\right]^{1/4}, \tag{5.1}$$

which varies along the flow. Thus the local Froude number differs from Fr_{geo} as the flow develops, and the direct relevance of Fr_{geo} to the entire flow is difficult to rationalise.

The predicted variation of Froude number along the flow also highlights the potential limitation of using a single constant value of the entrainment coefficient E along the entire length of the flow, as is commonly assumed when inferring entrainment values from experimental data. In particular, if the imposed initial momentum flux in the experiment causes the current to behave more like a jet very close to the source, this may modify the entrainment dynamics close to the source and require a correction to the critical level that would be predicted by a single constant value of E. An alternative hypothesis is that the entrainment coefficient is instead a function of the local Froude number. To investigate this hypothesis, the theoretical solutions must be modified to allow the entrainment coefficient to vary along the flow, with E given by an as-yet-undetermined function of the Froude number. A full investigation of the validity of these assumptions lies beyond the scope of the

https://doi.org/10.1017/jfm.2014.119 Published online by Cambridge University Press

present study. However, an experimental design that allows estimates of entrainment which account for local changes in Froude number along the current represents a compelling challenge for future work. The present theoretical framework offers a potentially valuable tool to contribute to such a goal.

6. Summary and discussion

We have developed a theoretical framework for modelling steady turbulent density currents flowing down a conical slope in a rotating system, for both the case of currents from an axisymmetric source of dense fluid and the case of a single-stream flow from a source of confined angular extent. As a demonstration of the utility of this modelling framework, we have presented solutions for flow with a constant entrainment coefficient and demonstrated that the flow evolves towards a critical level where there is no downslope flow. The inertia of the current causes it to overshoot a level of geostrophic balance between buoyancy and Coriolis forces, with the downslope propagation of the current subsequently arrested when the upslope component of the Coriolis force exceeds the downslope buoyancy forces. In contrast to earlier studies of flows with negligible inertia (for a summary, see Griffiths 1986; Shapiro & Hill 1997; Wirth 2009), our model of a turbulent entraining buoyancy-driven flow suggests that the state of azimuthal flow is attained even in the presence of basal friction. However, we expect our model to be adequate in simulating only the approach of the density current to its critical level, and not any subsequent propagation in a state of geostrophic balance as was considered by Shapiro & Hill (1997) and Wirth (2009). The steady model approximations break down at the critical level, as the plume thickness becomes large and violates the boundary layer approximation. Large gradients in thickness also generate significant gradients in hydrostatic pressure, which have been neglected in our model and will drive spreading of the current in both lateral and along-slope directions at the critical level. Because of this, we expect to observe a subsequent leakage of dense fluid down the slope. In fact, since the current does not transfer buoyancy downwards at the critical level, and in a statistical steady state the buoyancy flux should be constant at every depth level, the entire salt flux that enters at the source is transferred to the bottom of the tank through the transient leakage. Quantifying the transient leakage dynamics remains a difficult problem as it involves parameterisation of a transient turbulent Ekman layer subject to an overlying inertial flow, which remains an open question.

The modelling results described above do not explicitly characterise the Ekman layer dynamics, and we now evaluate this assumption for settings relevant to our laboratory experiments. Following the analysis of Wåhlin & Walin (2001), an appropriate viscous Ekman layer depth scale is $\delta_{Ek} \sim \sqrt{\nu/2f}$ where ν is the kinematic viscosity of the fluid, which yields 6×10^{-4} m $< \delta_{Ek} < 9 \times 10^{-4}$ m over the range of rotation rates considered in our laboratory experiments. The estimated Ekman layer thickness δ_{Ek} is smaller than the numerically predicted thickness b of the turbulent plume (see, for example, figure 2), which suggests that (2.1) captures the leading-order behaviour of the mass flux. However, a more complete theory might apply a higher-order correction of order δ_{Ek}/b to account for drainage in the Ekman layers resulting from the divergence of the Ekman transport (Wåhlin & Walin 2001). We can also investigate the potential role of Ekman drag. For example, Wobus *et al.* (2011) showed that the viscous Ekman layer drainage in transient gravity currents is not well characterised by the drag law (2.10). To test the robustness of the existence of a critical level in our model, we obtained further solutions using a different

https://doi.org/10.1017/jfm.2014.119 Published online by Cambridge University Press

parameterisation of the frictional Ekman drag motivated by the results in appendix B of Wilchinsky, Feltham & Holland (2007), who observed that drag is oriented at approximately 10° to the current trajectory. Our alternative drag law replaces (2.10) with a drag

$$\frac{\boldsymbol{\tau}}{\rho_0} = K_{ek}(w\cos\gamma + v\sin\gamma,\, v\cos\gamma - w\sin\gamma) \tag{6.1}$$

that varies linearly with the plume speed but is rotated by an angle γ relative to the flow. Note that this expression also recovers the drag for an Ekman layer generated by the geostrophic component of the flow (Shapiro & Zatsepin 1997), by setting $\gamma = -45°$ and $K_{ek} = 0.75\sqrt{2\nu f}$. For the experimental setting simulated in figure 2, we found only 0.7 % difference in the value of s_{cr} between solutions using (2.10) with $K = 2 \times 10^{-3}$ and solutions using (6.1) with a drag coefficient $K_{ek} = K \times 0.06$ m s^{-1} and turning angle $\gamma = -10°$. The latter parameters were chosen so that the drag parameterisations lead to similar magnitudes of $\boldsymbol{\tau}$ but differing directions. For significantly larger values of the drag coefficient, we found that the critical level still exists even when frictional forces have a component perpendicular to the flow, and the value s_{cr} depends on the friction coefficient K as well as on the angle to the current (results not illustrated here). Nevertheless, while appropriate parameterisations of the drag are still in question, the robust structure of the mean current and the distance at which it reaches the critical level allow us to infer fundamental properties of the turbulent fluxes that control the flow.

We derived an analytical solution for the special case of initial conditions with a constant buoyancy flux but negligible initial fluxes of mass and momentum delivered at the apex of the cone. This special solution serves as an attractor for general initial conditions, with the flow asymptotically approaching it as the current develops downslope. The attractor yields the prediction (3.22) for the dependence of the critical level on system parameters, which scales as $s_{cr} \propto \left(Q_B/Ef^3\right)^{1/4}$ in the limit of weak friction with $K/E \ll 1$. However, for experimental configurations with large rotation rates, the true solution does not closely approach the attractor before it reaches a critical level, below which the solution to the plume equations does not exist. In this case, we constructed an approximate solution by using an asymptotic expansion around the attractor. This correction to the solution satisfies the initial conditions and proved to be a reasonable approximation across a range of appropriate parameters. We have also described an analysis of a density current on a planar slope in a rotating frame (see appendix C), and this leads to qualitatively similar solutions. The analysis provides useful guidance in interpreting experiments with density currents from line sources of buoyancy released on planar slopes.

Guided by our theoretical understanding of the plume dynamics, we conducted a set of laboratory experiments for the case of a single-stream flow of confined angular extent. The experimental system exhibits behaviour consistent with the existence of a critical point. We explored experimentally the sensitivity of the critical point s_{cr} to the rotation rate of the reference frame. Furthermore, guided by our plume model solutions, we inferred the entrainment rate under the assumption that E is constant for each experiment. The data suggest that for rotationally dominated flow, the entrainment has the form $E \propto 1/f$, implying a suppression of turbulent mixing with increasing background rotation.

Such a dependence on rotation has previously been interpreted in terms of entrainment proportional to a geostrophic Froude number, $E \propto Fr_{geo} = \sqrt{g'/h}\tan\alpha/f$

https://doi.org/10.1017/jfm.2014.119 Published online by Cambridge University Press

(Wells 2007), which would be consistent with the slower geostrophic flow at higher rotation rates leading to reduced shear and thus reduced mixing. However, if we assume a spatially uniform value of the entrainment ratio E, the theoretical model considered here shows that the flow develops from initial conditions where the input Froude number is independent of f towards an attractor with a more complicated dependence on f. Hence, the local Froude number differs from the geostrophic Froude number Fr_{geo}, suggesting that the explanation for the observed reduction in entrainment with increased rotation rate is more complicated than previously anticipated.

The model developed here provides a theoretical structure that can be applied to future studies, allowing entrainment to be more precisely quantified in a well-defined experimental and theoretical setting. In particular, whereas previous experiments (Cenedese *et al.* 2004; Wells 2007; Cenedese & Adduce 2008) have sought to characterise entrainment as a function of Froude number, our theoretical solutions for constant entrainment demonstrate that the local Froude number evolves along the length of the flow. Whilst previous estimates of entrainment in rotating laboratory experiments have determined the mean entrainment for flows under given experimental conditions, our results suggest that the variation of Froude number along the flow may complicate attempts to infer a functional relationship $E(Fr)$ using a constant Froude number based on the initial conditions and/or purely geostrophic flow. Subject to suitable specification of an entrainment function E, our theory is applicable to a wide range of turbulent flows, from jets to purely buoyancy-driven currents. Further extensions motivated by oceanographic applications might also consider the role of downslope variations in hydrostatic pressure relevant to very shallow ocean slopes (Borenäs & Wåhlin 2000), or complications due to topographic steering by seafloor canyons and ridges (Wåhlin *et al.* 2008). A further intriguing possibility for future work is to extend the theory and experiments to consider flows with a shallow depth of ambient fluid and a large current thickness that induces a significant potential vorticity anomaly in the upper layer, thus providing a setting to study buoyancy-driven flows with an effective beta-plane approximation (G. Veronis, personal communication).

Acknowledgements

We thank three anonymous reviewers for their suggestions for improving the manuscript, and George Veronis for his illuminating comments on this work. All of the authors thank Yale University for support. J.S.W. thanks the John Simon Guggenheim Foundation, and a Royal Society Wolfson Research Merit Award for support.

Appendix A. Derivation of the plume equations

The plume model is derived from first principles by considering buoyancy-driven boundary layer flow on a cone as illustrated in figure 1. We present a derivation below for an isolated current of angular extent $\Delta\theta$, with the axisymmetric plume equations recovered as the special case of $\Delta\theta = 2\pi$. Starting from the Reynolds-averaged Navier–Stokes equations for rotating, buoyancy-driven flow in cylindrical coordinates (r, θ, z), we transform to a coordinate system (s, η, θ) where s is parallel and η is perpendicular to the conical surface. If the cone apex is at $\eta = s = 0$ and $r = z = 0$, then $r = s\cos\alpha + \eta\sin\alpha$, $z = -s\sin\alpha + \eta\cos\alpha$ and we denote the velocity by $\boldsymbol{u} = (u_s, u_\eta, u_\theta)$ in the

https://doi.org/10.1017/jfm.2014.119 Published online by Cambridge University Press

(s, η, θ) coordinate system. The transformed Navier–Stokes equations yield

$$\frac{1}{r}\frac{\partial}{\partial s}(ru_s^2)+\frac{1}{r}\frac{\partial}{\partial \eta}(ru_s u_\eta)+\frac{1}{r}\frac{\partial}{\partial \theta}(u_\theta u_s) = -\frac{1}{\rho_0}\frac{\partial \tilde{P}}{\partial s}+\frac{u_\theta^2\cos\alpha}{r}+2\Omega\cos\alpha u_\theta+\cdots + \frac{\rho}{\rho_0}g\sin\alpha+F_s, \tag{A 1}$$

$$\frac{1}{r}\frac{\partial}{\partial s}(ru_\theta u_s)+\frac{1}{r}\frac{\partial}{\partial \eta}(ru_\theta u_\eta)+\frac{1}{r}\frac{\partial}{\partial \theta}\left(u_\theta^2\right) = -\frac{1}{\rho_0 r}\frac{\partial \tilde{P}}{\partial \theta}-\frac{u_\theta(u_s\cos\alpha+u_\eta\sin\alpha)}{r}+\cdots - 2\Omega(u_s\cos\alpha+u_\eta\sin\alpha)+F_\theta, \tag{A 2}$$

$$\frac{1}{r}\frac{\partial}{\partial s}(ru_s u_\eta)+\frac{1}{r}\frac{\partial}{\partial \eta}(ru_\eta^2)+\frac{1}{r}\frac{\partial}{\partial \theta}(u_\theta u_\eta) = -\frac{1}{\rho_0}\frac{\partial \tilde{P}}{\partial \eta}+\frac{u_\theta^2\sin\alpha}{r}+\cdots + 2\Omega\sin\alpha u_\theta-\frac{\rho}{\rho_0}g\cos\alpha+F_\eta, \tag{A 3}$$

$$\frac{1}{r}\frac{\partial}{\partial s}(ru_s)+\frac{1}{r}\frac{\partial}{\partial \eta}(ru_\eta)+\frac{1}{r}\frac{\partial u_\theta}{\partial \theta} = 0 \tag{A 4}$$

and

$$\frac{1}{r}\frac{\partial}{\partial s}(r\rho u_s)+\frac{1}{r}\frac{\partial}{\partial \eta}(r\rho u_\eta)+\frac{1}{r}\frac{\partial}{\partial \theta}(\rho u_\theta)=0, \tag{A 5}$$

where $\tilde{P}=P-\Omega^2 r^2/2$ is an effective pressure that includes the fluid pressure P and the centrifugal contribution from the rotating reference frame. The frictional force $\boldsymbol{F}=(F_s, F_\eta, F_\theta)$ includes both viscous shear stresses and eddy momentum fluxes due to the time-average of turbulent fluctuations in velocity:

$$\boldsymbol{F}=\boldsymbol{\nabla}\cdot\tau=\nu\nabla^2\boldsymbol{u}-\boldsymbol{\nabla}\cdot\left(\overline{\boldsymbol{u}'\boldsymbol{u}'}\right). \tag{A 6}$$

The density current has a shallow characteristic thickness H compared to the distance L flowed along the slope, and so we apply a boundary layer approximation under the condition $L\gg H$ (Schlichting 1968). This yields

$$\frac{1}{r}\frac{\partial}{\partial s}(ru_s^2)+\frac{1}{r}\frac{\partial}{\partial \eta}(ru_s u_\eta)+\frac{1}{r}\frac{\partial}{\partial \theta}(u_\theta u_s) = \frac{u_\theta^2\cos\alpha}{r}+2\Omega\cos\alpha u_\theta+\cdots + \frac{\rho-\rho_0}{\rho_0}g\sin\alpha+\frac{1}{r}\frac{\partial}{\partial \eta}\left(r\tau_{\eta s}\right), \tag{A 7}$$

$$\frac{1}{r}\frac{\partial}{\partial s}(ru_\theta u_s)+\frac{1}{r}\frac{\partial}{\partial \eta}(ru_\theta u_\eta)+\frac{1}{r}\frac{\partial}{\partial \theta}u_\theta^2 = -\frac{u_\theta u_s\cos\alpha}{r}-2\Omega\cos\alpha u_s+\frac{1}{r}\frac{\partial}{\partial \eta}\left(r\tau_{\eta\theta}\right), \tag{A 8}$$

$$\frac{1}{r}\frac{\partial}{\partial s}(ru_s)+\frac{1}{r}\frac{\partial}{\partial \eta}(ru_\eta)+\frac{1}{r}\frac{\partial u_\theta}{\partial \theta} = 0 \tag{A 9}$$

and

$$\frac{1}{r}\frac{\partial}{\partial s}(r\rho u_s)+\frac{1}{r}\frac{\partial}{\partial \eta}(r\rho u_\eta)+\frac{1}{r}\frac{\partial}{\partial \theta}(\rho u_\theta)=0, \tag{A 10}$$

where ρ_0 is the environmental density far away from the current and $\tau_{\eta s}$ and $\tau_{\eta\theta}$ are components of τ. We have here neglected the contribution from downslope

https://doi.org/10.1017/jfm.2014.119 Published online by Cambridge University Press

gradients in hydrostatic pressure, which can be justified provided $H \ll L \tan\alpha$ (following Borenäs & Wåhlin 2000). In our theoretical results this is a self-consistent approximation in agreement with our experimental observations of flows on relatively steep slopes, but it may break down in certain flows on very shallow slopes in the ocean (Borenäs & Wåhlin 2000). We also assume that the azimuthal gradients in hydrostatic pressure can be neglected, consistent with an assumed constant angular width.

Plume equations can be derived by averaging (A 7)–(A 10) azimuthally and normal to the slope. We define the effective plume width b, downslope velocity w, azimuthal velocity v and density ρ according to (2.5)–(2.8), where the current has angular extent $\Delta\theta$ and the cone has local radius r_s. One could interpret these definitions in terms of piecewise-constant 'top-hat' profiles over a rectangle in (η, θ) space, although such an assumption is not required. Under the assumption of self-similarity, the other integral terms arising are approximated by

$$\int_0^{2\pi}\int_0^{\infty} u_\theta^2 \,\mathrm{d}\eta\,\mathrm{d}\theta = \beta_1 b v^2 \Delta\theta, \qquad \int_0^{2\pi}\int_0^{\infty} r u_\theta \,\mathrm{d}\eta\,\mathrm{d}\theta = \beta_2 b v r_s \Delta\theta \tag{A 11}$$

and

$$\int_0^{2\pi}\int_0^{\infty} u_\theta u_s \,\mathrm{d}\eta\,\mathrm{d}\theta = \beta_3 b w v \Delta\theta, \tag{A 12}$$

where the shape factors β_1, β_2 and β_3 are constants, with $\beta_1 = \beta_2 = \beta_3 = 1$ for 'top-hat' profiles (Linden 2000). Finally, we write the effective entrainment velocity v_e as

$$\int_0^{2\pi} r u_\eta \,|_{\eta=\infty}\,\mathrm{d}\theta \cong -\Delta\theta r_s v_e \tag{A 13}$$

and the effective drag components as

$$\int_0^{2\pi} r\tau_{\eta s}\,\mathrm{d}\theta \cong \Delta\theta r_s \tau_s \quad \text{and} \quad \int_0^{2\pi} r\tau_{\eta\theta}\,\mathrm{d}\theta \cong \Delta\theta r_s \tau_\theta. \tag{A 14}$$

Using the above definitions and assuming $\beta_1 = \beta_2 = \beta_3 = 1$, a domain integration $\int_0^{2\pi}\int_0^{\infty}(\cdot) r\,\mathrm{d}\eta\,\mathrm{d}\theta$ of (A 7)–(A 10) yields

$$\frac{\mathrm{d}}{\mathrm{d}s}(b w^2 r_s) - b v^2 \cos\alpha = 2\Omega \cos\alpha b v r_s + \frac{\tilde{\rho} - \rho_0}{\rho_0} b r_s g \sin\alpha - r_s \tau_s - \frac{\mathrm{d}(\ln\Delta)\theta}{\mathrm{d}s} b w^2 r_s, \tag{A 15}$$

$$\frac{\mathrm{d}}{\mathrm{d}s}(b w v r_s) + b w v \cos\alpha = -2\Omega \cos\alpha b w r_s - r_s \tau_\theta - \frac{\mathrm{d}(\ln\Delta\theta)}{\mathrm{d}s} b v w r_s, \tag{A 16}$$

$$\frac{\mathrm{d}}{\mathrm{d}s}(b w r_s) = r_s v_e - \frac{\mathrm{d}\ln(\Delta\theta)}{\mathrm{d}s} b w r_s \tag{A 17}$$

and

$$\frac{\mathrm{d}}{\mathrm{d}s}\left(\frac{\rho - \rho_0}{\rho_0} b r_s w\right) g \sin\alpha = -\frac{\mathrm{d}\ln(\Delta\theta)}{\mathrm{d}s} \frac{\tilde{\rho} - \rho_e}{\rho_0} b w r_s g \sin\alpha, \tag{A 18}$$

which after some algebraic manipulations are equivalent to (2.1)–(2.4).

https://doi.org/10.1017/jfm.2014.119 Published online by Cambridge University Press

In the axisymmetric case the flow is 2π-periodic with $\Delta\theta = 2\pi$, so that $\mathrm{d}(\ln \Delta\theta)/\mathrm{d}s = 0$ and the system is closed. For an isolated plume of angular extent $\Delta\theta < 2\pi$, a separate closure assumption is required to determine $\Delta\theta$ and describe the physical processes responsible for azimuthal widening of the current. However, whenever the terms involving $\mathrm{d}(\ln \Delta\theta)/\mathrm{d}s$ are small, the isolated plume evolves according to the same leading-order dynamics as in the axisymmetric case. Formally this condition can be estimated from

$$\frac{\mathrm{d}\,(\ln \Delta\theta)}{\mathrm{d}s} \ll \frac{\mathrm{d}\,[\ln\,(bws)]}{\mathrm{d}s}, \quad \frac{\mathrm{d}\left[\ln(bw^2s)\right]}{\mathrm{d}s}, \quad \frac{\mathrm{d}\,[\ln(bwvs)]}{\mathrm{d}s}, \quad \frac{\mathrm{d}\left(\ln\left[bws(\tilde{\rho}-\rho_0)\right]\right)}{\mathrm{d}s}, \tag{A 19}$$

which is the condition required for the final term in each of (A 15)–(A 18) to be small compared with the corresponding first term, noting that $r_s = s\cos\alpha$. Whenever (A 19) is satisfied, the single-stream flow of an isolated plume forms an angular subsection of the corresponding axisymmetric flow. Some of the fluxes in (A 19) are challenging to estimate directly from our experimental data, but we can derive an approximate indicator of the relative magnitudes as follows. Our plume model assumes that the total downslope buoyancy flux is conserved, so we focus on the mass and momentum balances here. By summing (A 15) multiplied by bw^2r_s and (A 16) multiplied by $bwvr_s$, we can derive an alternative constraint on the downslope momentum flux, so that the second condition in (A 19) can be replaced by the more easily estimated

$$\frac{\mathrm{d}\,(\ln \Delta\theta)}{\mathrm{d}s} \ll \frac{\mathrm{d}\left\{\ln\left[b^2w^2(v^2+w^2)s^2\right]\right\}}{\mathrm{d}s}. \tag{A 20}$$

The attractor solution (3.10)–(3.12) derived in the main text predicts that the fluxes satisfy

$$bws \propto s^{5/3}, \quad bwvs \propto s^{8/3}, \quad b^2w^2(v^2+w^2)s^2 \propto s^{8/3}, \tag{A 21}$$

where the final term corresponds to a dimensional form of the variable F in (3.11). Taking logarithms and then derivatives with respect to s yields

$$\frac{\mathrm{d}\,[\ln\,(bws)]}{\mathrm{d}s} = \frac{5}{3s}, \quad \frac{\mathrm{d}\,[\ln\,(bwvs)]}{\mathrm{d}s} = \frac{8}{3s}, \quad \frac{\mathrm{d}\left\{\ln\left[b^2w^2(v^2+w^2)s^2\right]\right\}}{\mathrm{d}s} = \frac{8}{3s}. \tag{A 22}$$

Thus we estimate that the first three conditions in (A 19) are likely to be a reasonable approximation if

$$\frac{\mathrm{d}\,(\ln \Delta\theta)}{\mathrm{d}s} \ll \frac{5}{3s} \tag{A 23}$$

or, equivalently, $\mathrm{d}(\ln \Delta\theta)/\mathrm{d}(\ln s) \ll 5/3$. The experimental comparison shows that the relative magnitude of this term is on average 15 % (having a maximum at 25 %), which justifies our neglect of this term in the equations.

Appendix B. Fixed point analysis

In order to determine the fixed points and attractors for the system (3.6)–(3.8), we make the substitutions

$$x = FE^{-2/3}\xi^{-8/3}, \quad y = P^2E^{-4/3}\xi^{-10/3}, \quad z = VE^{-2/3}\xi^{-8/3} \tag{B 1}$$

https://doi.org/10.1017/jfm.2014.119 Published online by Cambridge University Press

and define $\zeta = \ln \xi$, yielding

$$\frac{\mathrm{d}x}{\mathrm{d}\zeta} = -\frac{8}{3}x + 2\sqrt{y} - \frac{2K}{E}\frac{x^{3/2}}{y}, \tag{B 2}$$

$$\frac{\mathrm{d}y}{\mathrm{d}\zeta} = 2\sqrt{x} - \frac{10}{3}y \tag{B 3}$$

and

$$\frac{\mathrm{d}z}{\mathrm{d}\zeta} = -\frac{11}{3}z + \sqrt{y} - \frac{K}{E}\frac{z\sqrt{x}}{y}. \tag{B 4}$$

Note that this system can be treated as closed in the following manner. Consider z as determined from (B 4) to be slaved to x and y as determined from (B 2) and (B 3). Setting $\mathrm{d}x/\mathrm{d}\zeta = \mathrm{d}y/\mathrm{d}\zeta = \mathrm{d}z/\mathrm{d}\zeta = 0$ yields the unique fixed point

$$x = \bar{x} \equiv \frac{9}{2^{8/3}5^{2/3}\left(1 + \frac{5}{4}\frac{K}{E}\right)^{4/3}}, \tag{B 5}$$

$$y = \bar{y} \equiv \frac{9}{2^{4/3}5^{4/3}\left(1 + \frac{5}{4}\frac{K}{E}\right)^{2/3}}, \tag{B 6}$$

$$z = \bar{z} \equiv \frac{9}{2^{2/3}5^{2/3}11\left(1 + \frac{5}{4}\frac{K}{E}\right)^{1/3}\left(1 + \frac{5}{11}\frac{K}{E}\right)} \tag{B 7}$$

corresponding to the special solution (3.10)–(3.12).

To determine the stability, we linearise about the fixed point by letting $x = \bar{x} + \chi_x$, $y = \bar{y} + \chi_y$ and $z = \bar{z} + \chi_z$. Writing $\chi = (\chi_x, \chi_y, \chi_z)$ with $|\chi| \ll 1$, this yields the linearised system

$$\frac{\partial \chi}{\partial \zeta} = D\chi, \tag{B 8}$$

where

$$D = \begin{pmatrix} -\frac{8}{3} - \frac{3\sqrt{\bar{x}}}{\bar{y}}\frac{K}{E} & \frac{1}{\sqrt{\bar{y}}} + \frac{2\bar{x}^{3/2}}{\bar{y}^2}\frac{K}{E} & 0 \\ \frac{1}{\sqrt{\bar{x}}} & -\frac{10}{3} & 0 \\ -\frac{\bar{z}}{2\bar{y}\sqrt{\bar{x}}}\frac{K}{E} & \frac{1}{2\sqrt{\bar{y}}} + \frac{\bar{z}\sqrt{\bar{x}}}{\bar{y}^2}\frac{K}{E} & -\frac{11}{3} - \frac{\sqrt{\bar{x}}}{\bar{y}}\frac{K}{E} \end{pmatrix}. \tag{B 9}$$

Upon substituting for $\bar{x}$, $\bar{y}$ and $\bar{z}$ we find that the eigenvalue of the matrix D corresponding to the evolution of the slaved coordinate z is $\lambda = -11/3 - 5K/(3E)$, which is always negative. The remaining two eigenvalues of D are given by $\lambda = -b/2 \pm \sqrt{b^2 - 4c}/2$ where

$$b = 6 + 5\frac{K}{E}, \quad c = \frac{20}{3} + \frac{25}{3}\frac{K}{E}. \tag{B 10}$$

https://doi.org/10.1017/jfm.2014.119 Published online by Cambridge University Press

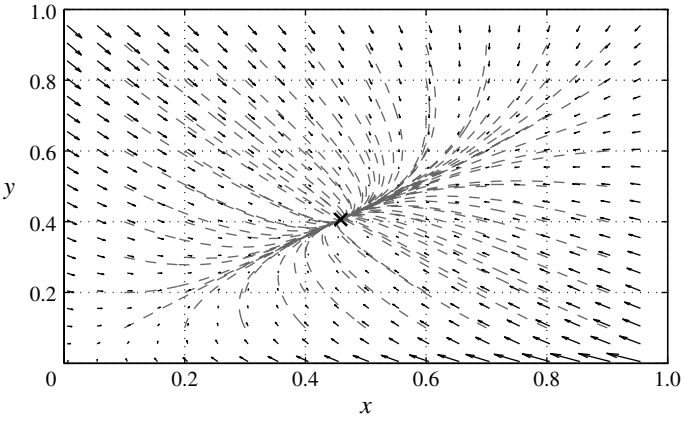


FIGURE 8. Convergence of all trajectories in (x, y) phase space to the fixed point (indicated by a cross) corresponding to (3.10)–(3.12), for the special case where $K = 0$. Short arrows show the local flow direction $(\mathrm{d}x/\mathrm{d}\zeta, \mathrm{d}y/\mathrm{d}\zeta)$, with example trajectories indicated by dashed curves.

Since $0 < c < b^2/4$, these eigenvalues are negative and the fixed point is asymptotically stable. Because the closed system in (x, y) is two-dimensional, the unique fixed point serves as an attractor for all solution trajectories with different initial conditions. An example of the evolution of the (x, y) trajectories corresponding to the closed subsystem (B 2) and (B 3) is illustrated in figure 8.

Appendix C. Rotating density currents on a planar slope

The plume model can also be generalised to rotating density currents on a planar slope inclined at an angle α to the horizontal. The planar slope limit can be either derived from first principles using the method of appendix A (not detailed here) or recovered from the axisymmetric model (2.1)–(2.4) by considering the conceptual limit of a large radius of curvature $r_s \to \infty$, but with the equivalent plume width $a = r_s\Delta\theta$ remaining finite. In this planar-slope limit the downslope fluxes of mass, downslope momentum, across-slope momentum and buoyancy are now described by

$$\frac{\mathrm{d}}{\mathrm{d}s}(abw) = aE\sqrt{v^2 + w^2}, \tag{C 1}$$

$$\frac{\mathrm{d}}{\mathrm{d}s}\left(abw^2\right) = abg\sin\alpha\frac{\rho - \rho_0}{\rho_0} - abfv - aKw\sqrt{v^2 + w^2}, \tag{C 2}$$

$$\frac{\mathrm{d}}{\mathrm{d}s}(abwv) = abfw - aKv\sqrt{v^2 + w^2} \tag{C 3}$$

and

$$\frac{\mathrm{d}}{\mathrm{d}s}\left(abw\frac{\rho - \rho_0}{\rho_0}\right) = 0, \tag{C 4}$$

where s is the downslope distance, and we define the across-slope distance x along isobaths. In this planar-slope limit, the effective plume width b, downslope plume

https://doi.org/10.1017/jfm.2014.119 Published online by Cambridge University Press

velocity w, across-slope velocity v and mean density ρ are defined in terms of the fluxes

$$\int_{-\infty}^{\infty}\int_{0}^{\infty} u_s \,\mathrm{d}\eta\,\mathrm{d}x \equiv abw, \tag{C 5}$$

$$\int_{-\infty}^{\infty}\int_{0}^{\infty} u_s^2 \,\mathrm{d}\eta\,\mathrm{d}x \equiv abw^2, \tag{C 6}$$

$$\int_{-\infty}^{\infty}\int_{0}^{\infty} u_x u_s \,\mathrm{d}\eta\,\mathrm{d}x \equiv abvw \tag{C 7}$$

and

$$\int_{-\infty}^{\infty}\int_{0}^{\infty} u_s \frac{\tilde{\rho}-\rho_0}{\rho_0}\,\mathrm{d}\eta\,\mathrm{d}x \equiv abw\frac{\rho-\rho_0}{\rho_0}, \tag{C 8}$$

where $u_x(x, s, \eta)$ is the across-slope velocity field in planar coordinates. Similarly to the axisymmetric case, we neglect lateral spreading driven by across-slope variations in hydrostatic pressure and mixing at the current sides, so that the planar current width a is assumed constant. After dividing (C 1)–(C 4) through by the constant a, the resulting differential equations can describe either flows from an infinite line source at $s = s_I$ or the path-lines of a single-stream flow of constant width from a localised line source at $s = s_I$ with effective width $0 < x < a$.

A leading-order similarity solution and asymptotic corrections to account for initial conditions can be derived in a similar fashion to the axisymmetric case, which we summarise briefly below. The downslope buoyancy flux per unit width, Q_B, is conserved, with (C 4) integrating to yield

$$bwg\sin\alpha\,\frac{\rho-\rho_0}{\rho_0} = Q_B = \text{constant}. \tag{C 9}$$

We define

$$\xi = \frac{sf}{Q_B^{1/3}}, \quad P = \frac{bwf}{Q_B^{2/3}}, \quad W = \frac{bw^2 f}{Q_B}, \quad V = \frac{bwvf}{Q_B}, \tag{C 10}$$

which represent dimensionless downslope distance and downslope fluxes of mass, downslope momentum and across-slope momentum, respectively. Defining the variable $F = V^2 + W^2$ for convenience, the governing equations (C 1)–(C 3) combine to give

$$\dot{P} = E\frac{\sqrt{F}}{P}, \tag{C 11}$$

$$\dot{F} = 2P - 2K\frac{F^{3/2}}{P^2} \tag{C 12}$$

and

$$\dot{V} = P - KV\frac{\sqrt{F}}{P^2}, \tag{C 13}$$

where a dot denotes $\mathrm{d}/\mathrm{d}\xi$. The leading-order dynamics is characterised by a special solution for a line source of buoyancy with negligible initial fluxes of mass and momentum, and with initial conditions $P = V = W = F = 0$ imposed at a particular

https://doi.org/10.1017/jfm.2014.119 Published online by Cambridge University Press

downslope position $\xi = \xi_0$. We obtain power-law similarity solutions

$$P = \frac{E^{2/3}}{\left(1 + \dfrac{K}{E}\right)^{1/3}} (\xi - \xi_0)\,, \tag{C 14}$$

$$F = \frac{E^{2/3}}{\left(1 + \dfrac{K}{E}\right)^{4/3}} (\xi - \xi_0)^2 \tag{C 15}$$

and

$$V = \frac{E^{2/3}}{2\left(1 + \dfrac{K}{E}\right)^{1/3}\left(1 + \dfrac{K}{2E}\right)} (\xi - \xi_0)^2\,. \tag{C 16}$$

Comparing the power-law exponents in the solutions (C 14)–(C 16) with those in (3.10)–(3.12), we see that the downslope fluxes of mass and across-slope momentum grow more slowly in planar geometry than their axisymmetric counterparts. However, the flow in planar geometry develops in a qualitatively similar fashion to the axisymmetric case, and in particular exhibits a critical level $s = s_{cr}$ where the downslope flow ceases ($w = 0$). The critical level is determined by solving $W^2 = F - V^2 = 0$ for $\xi = \xi_{cr}$, which yields

$$s_{cr} - s_0 = 2\frac{\left(1 + \dfrac{K}{2E}\right)}{\left(1 + \dfrac{K}{E}\right)^{1/3}} \left(\frac{Q_B}{Ef^3}\right)^{1/3} \tag{C 17}$$

in dimensional units.

The similarity solution (C 14)–(C 16) is exact for initial conditions with $P = V = F = 0$ at $\xi = \xi_0$, but similarly to the axisymmetric case we also expect this solution to capture the leading-order asymptotic behaviour for large ξ when more general initial conditions are used. However, the similarity solution does not satisfy all possible initial conditions with fluxes $P = P_0$, $F = F_0$ and $V = V_0$ imposed at $\xi = \xi_I$. In a similar fashion to the axisymmetric case, we therefore derive linearised corrections to the similarity solution for planar geometry. The resulting combination of similarity solution plus leading-order corrections can be used to approximate solutions with non-zero initial fluxes of mass and momentum imposed at some $\xi = \xi_I$, with the similarity solution describing the asymptotic leading-order behaviour for larger ξ. Following the method of § 3.3, we perturb the similarity solution by letting

$$P = P_a + \hat{P}, \quad F = F_a + \hat{F}, \quad V = V_a + \hat{V}, \tag{C 18}$$

where $P = P_a$, $F = F_a$ and $V = V_a$ are given by (C 14)–(C 16), with ξ_0 being an as-yet-undetermined virtual origin (see Hunt & Kaye 2001, for example), and $\hat{P} \ll P_a$, $\hat{F} \ll F_a$ and $\hat{V} \ll V_a$. Setting $K = 0$ again for mathematical simplicity and linearising (C 11)–(C 13), we find that

$$\frac{\mathrm{d}\hat{P}}{\mathrm{d}\xi} = \frac{\hat{F}}{2\,(\xi - \xi_0)^2} - \frac{\hat{P}}{(\xi - \xi_0)}, \tag{C 19}$$

$$\frac{\mathrm{d}\hat{F}}{\mathrm{d}\xi} = 2\hat{P} \tag{C 20}$$

https://doi.org/10.1017/jfm.2014.119 Published online by Cambridge University Press

and

$$\frac{\mathrm{d}\hat{V}}{\mathrm{d}\xi} = \hat{P}. \tag{C 21}$$

Combining (C 19) and (C 20) results in the second-order differential equation

$$(\xi - \xi_0)^2 \frac{\mathrm{d}^2\hat{F}}{\mathrm{d}\xi^2} + (\xi - \xi_0) \frac{\mathrm{d}\hat{F}}{\mathrm{d}\xi} - \hat{F} = 0, \tag{C 22}$$

which has a regular singular point at $\xi = \xi_0$. The resulting solution is

$$\hat{F} = B_1 (\xi - \xi_0) + \frac{B_2}{(\xi - \xi_0)}, \tag{C 23}$$

$$\hat{P} = \frac{B_1}{2} - \frac{B_2}{2 (\xi - \xi_0)^2}, \tag{C 24}$$

$$\hat{V} = \frac{B_1 (\xi - \xi_0)}{2} - \frac{B_2}{2 (\xi - \xi_0)} + B_3, \tag{C 25}$$

where the constants $B_{1,2,3}$ are chosen so that the total solution (C 18) satisfies the initial conditions for F, P and V at $\xi = \xi_I > \xi_0$. For this approximate solution, there is still the freedom to choose the virtual origin correction ξ_0. One could potentially choose ξ_0 so that the initial conditions $P = P_0$, $F = F_0$ and $V = V_0$ imposed at $\xi = \xi_I$ lie close to the similarity solution, thus improving the accuracy of the linearisation. For example, choosing ξ_0 so that $P_a(\xi_I) = P_0$ would be a convenient and simple choice. Alternatively, one might try to determine a virtual origin correction explicitly by using analytical methods (Hunt & Kaye 2001), although such an analysis has not been attempted here. The sum of the similarity solution (C 14)–(C 16) and the correction (C 23)–(C 25) then constitutes an approximate solution that satisfies the initial conditions and captures the leading-order asymptotic behaviour for large ξ.

REFERENCES

Baines, W. D. & Turner, J. S. 1969 Turbulent buoyant convection from a source in a confined region. *J. Fluid Mech.* **37**, 51–80.

Borenäs, K. & Wåhlin, A. K. 2000 Limitations of the streamtube model. *Deep-Sea Res.* I **47**, 1333–1350.

Carmack, E. C. 2000 The Arctic Ocean's freshwater budget: sources, storage and export. In *Proceedings of the NATO Advanced Research Workshop on The Freshwater Budget of the Arctic Ocean* (ed. E. L. Lewis), pp. 91–126. Kluwer.

Cenedese, C. & Adduce, C. 2008 Mixing in a density-driven current flowing down a slope in a rotating fluid. *J. Fluid Mech.* **604**, 369–388.

Cenedese, C. & Adduce, C. 2010 A new parameterisation for entrainment in overflows. *J. Phys. Oceanogr.* **40** (8), 1835–1850.

Cenedese, C., Whitehead, J. A., Ascarelli, T. A. & Ohiwa, M. 2004 A dense current flowing down a sloping bottom in a rotating fluid. *J. Phys. Oceanogr.* **34** (1), 188–203.

Cleveland, W. S. 1981 LOWESS: a programme for smoothing scatterplots by robust locally weighted regression. *Am. Statist.* **35** (1), 54.

Ellison, T. H. & Turner, J. S. 1959 Turbulent entrainment in stratified flows. *J. Fluid Mech.* **6** (3), 423–448.

Garratt, J. R., Howells, P. A. C. & Kowalczyk, E. 1989 The behaviour of dry cold fronts travelling along a coastline. *Mon. Weath. Rev.* **117** (6), 1208–1220.

https://doi.org/10.1017/jfm.2014.119 Published online by Cambridge University Press

GRIFFITHS, R. W. 1986 Gravity currents in rotating systems. *Annu. Rev. Fluid Mech.* **18**, 59–89.

HUGHES, G. O. & GRIFFITHS, R. W. 2006 A simple convective model of the global overturning circulation, including effects of entrainment into sinking regions. *Ocean Model.* **12** (1–2), 46–79.

HUNT, G. R. & KAYE, N. G. 2001 Virtual origin correction for lazy turbulent plumes. *J. Fluid Mech.* **435**, 377–396.

HUPPERT, H. E. 2006 Gravity currents: a personal perspective. *J. Fluid Mech.* **554**, 299–322.

IVANOV, V. V., SHAPIRO, G. I., HUTHNANCE, J. M., ALEYNIK, D. L. & GOLOVIN, P. N. 2004 Cascades of dense water around the world ocean. *Prog. Oceanogr.* **60** (1), 47–98.

LANE-SERFF, G. F. & BAINES, P. G. 1998 Eddy formation by dense flows on slopes in a rotating fluid. *J. Fluid Mech.* **363**, 229–252.

LIGNIERES, F., CATALA, C. & MANGENEY, A. 1996 Angular momentum transfer in pre-main-sequence stars of intermediate mass. *Astron. Astrophys.* **314** (2), 465–476.

LINDEN, P. F. 2000 Convection in the environment. In *Perspectives in Fluid Mechanics*, chap. 6, pp. 303–321. Cambridge University Press.

MCKEE, C. F. & OSTRIKER, E. C. 2007 Theory of star formation. *Annu. Rev. Astron. Astrophys.* **45**, 565–687.

MONAGHAN, J. J. 2007 Gravity current interaction with interfaces. *Annu. Rev. Fluid Mech.* **39**, 245–261.

MORTON, B. R., TAYLOR, G. I. & TURNER, J. S. 1956 Turbulent gravitational convection from maintained and instantaneous sources. *Proc. R. Soc. Lond.* A **234** (1196), 1–32.

NOF, D. 1983 The translation of isolated cold eddies on a sloping bottom. *Deep-Sea Res.* A **30** (2), 171–182.

PRATT, L. J., RIEMENSCHNEIDER, U. & HELFRICH, K. R. 2007 A transverse hydraulic jump in a model of the Faroe Bank Channel outflow. *Ocean Model.* **19**, 1–9.

PRICE, J. F. & BARINGER, M. O. 1994 Outflows and deep-water production by marginal seas. *Prog. Oceanogr.* **33** (3), 161–200.

PRINCEVAC, M., FERNANDO, H. J. S. & WHITEMAN, C. D. 2005 Turbulent entrainment into natural gravity-driven flows. *J. Fluid Mech.* **533**, 259–268.

RIEUTORD, M. & ZAHN, J. P. 1995 Turbulent plumes in stellar convective envelopes. *Astron. Astrophys.* **296** (1), 127–138.

SCHLICHTING, H. 1968 *Boundary Layer Theory*. 6th edn. McGraw Hill.

SHAPIRO, G. I. & HILL, A. E. 1997 Dynamics of dense water cascades at the shelf edge. *J. Phys. Oceanogr.* **27** (11), 2381–2394.

SHAPIRO, G. I. & ZATSEPIN, A. G. 1997 Gravity current down a steeply inclined slope in a rotating fluid. *Ann. Geophys.* **15**, 366–374.

SIMPSON, J. E. 1997 *Gravity Currents in the Environment and the Laboratory*. Cambridge University Press.

SMITH, P. C. 1975 A streamtube model for bottom boundary currents in the ocean. *Deep-Sea Res. Oceanogr. Abstr.* **22** (12), 853–873.

SUTHERLAND, B. R., NAULT, J., YEWCHUK, K. & SWATERS, G. E. 2004 Rotating dense currents on a slope. Part 1. Stability. *J. Fluid Mech.* **508**, 241–264.

TAYLOR, G. I. 1920 Tidal friction in the Irish Sea. *Phil. Trans. R. Soc. Lond.* A **220**, 1–33.

TIMMERMANS, M. -L., FRANCIS, J., PROSHUTINSKY, A. & HAMILTON, L. 2009 Taking stock of Arctic sea ice and climate. *Bull. Am. Meteorol. Soc.* **90** (9), 1351–1353.

TURNER, J. S. 1986 Turbulent entrainment: the development of the entrainment assumption, and its application to geophysical flows. *J. Fluid Mech.* **173**, 431–471.

WÅHLIN, A. K. & CENEDESE, C. 2006 How entraining density currents influence the stratification in a one-dimensional ocean basin. *Deep-Sea Res.* II **53** (1–2), 172–193.

WÅHLIN, A. K., DARELIUS, E., CENEDESE, C. & LANE-SERFF, G. F. 2008 Laboratory observations of enhanced entrainment in dense overflows in the presence of submarine canyons and ridges. *Deep-Sea Res.* I **55**, 737–750.

WÅHLIN, A. K. & WALIN, G. 2001 Downward migration of dense bottom currents. *Environ. Fluid Mech.* **1**, 257–279.

https://doi.org/10.1017/jfm.2014.119 Published online by Cambridge University Press

WELLS, M. G. 2007 Influence of Coriolis forces on turbidity currents and sediment deposition. In *Particle-Laden Flow: From Geophysical to Kolmogorov Scales* (ed. B. J. Geurts, H. Clercx & W. Uijttewaal), vol. 11, pp. 331–343. Springer.

WELLS, M. G., CENEDESE, C. & CAULFIELD, C. P. 2010 The relationship between flux coefficient and entrainment ratio in density currents. *J. Phys. Oceanogr.* **40** (12), 2713–2727.

WELLS, M. G. & WETTLAUFER, J. S. 2005 Two-dimensional density currents in a confined basin. *Geophys. Astrophys. Fluid Dyn.* **99** (3), 199–218.

WELLS, M. G. & WETTLAUFER, J. S. 2007 The long-term circulation driven by density currents in a two-layer stratified basin. *J. Fluid Mech.* **572**, 37–58.

WILCHINSKY, A. V., FELTHAM, D. L. & HOLLAND, P. R. 2007 The effect of a new drag-law parameterisation on ice shelf water plume dynamics. *J. Phys. Oceanogr.* **37** (7), 1778–1792.

WIRTH, A. 2009 On the basic structure of oceanic gravity currents. *Ocean Dyn.* **59** (4), 551–563.

WIRTH, A. 2011 Estimation of friction parameters in gravity currents by data assimilation in a model hierarchy. *Ocean Sci. Discus.* **8** (1), 159–187.

WOBUS, F., SHAPIRO, G. I., MAQUEDA, M. A. M. & HUTHNANCE, J. M. 2011 Numerical simulations of dense water cascading on a steep slope. *J. Mar. Res.* **69**, 391–415.

YOUDIN, A. N. & SHU, F. H. 2002 Planetesimal formation by gravitational instability. *Astrophys. J.* **580** (1), 494–505.

https://doi.org/10.1017/jfm.2014.119 Published online by Cambridge University Press